Metasomatic effect of Li-bearing aplite-pegmatites on psammitic and pelitic metasediments: Geochemical constraints on critical raw material exploration at the Fregeneda–Almendra Pegmatite Field (Spain and Portugal)

Jon Errandonea-Martin [a],[*], Idoia Garate-Olave [a], Encarnación Roda-Robles [a], Joana Cardoso-Fernandes [b],[c], Alexandre Lima [b],[c], Maria dos Anjos Ribeiro [b],[c], Ana Cláudia Teodoro [b],[c]

[a] *Department of Geology, Faculty of Science and Technology, University of the Basque Country UPV/EHU, Barrio Sarriena s/n, Leioa 48940, Spain*
[b] *Department of Geosciences, Environment and Spatial Planning, Faculty of Sciences, University of Porto, Rua Campo Alegre, Porto 4169-007, Portugal*
[c] *Institute of Earth Sciences (ICT), Pole of University of Porto, Porto 4169-007, Portugal*

ARTICLE INFO

ABSTRACT

Fluid-assisted mass transfer and re-equilibration of mineral phases are common consequences of metasomatism associated with igneous intrusions. The addition and/or removal of chemical components in these environments may result in the generation of metasomatic aureoles, which can be recognized by their mineralogy and geochemistry. Due to an increasing demand for critical raw materials used in green energy technologies, rare-element granitic pegmatites have seen renewed interest in the mineral exploration industry. Granitic pegmatites represent potential sources of critical commodities and geochemical studies of their related aureoles help to advance techniques in exploration targeting. Moreover, the role and timing of fluid exsolution during magmatic–hydrothermal evolution in granitic–pegmatitic systems and concomitant element mobility remain highly debated.

We present a prospect-scale systematic study of geochemical haloes generated by LCT (Li-Cs-Ta) family pegmatite dykes from the Fregeneda–Almendra Pegmatite Field, in the Central Iberian Zone of the Iberian Massif (Spain and Portugal). To understand the magnitude of metasomatic processes linked to these intrusions, we performed whole-rock mass-balance calculation of element gains and losses in variably metasomatized psammitic and pelitic host metasediments. The results show that F, B, Li, Rb, Cs, Sn, Be, Tl, As, W and S ($\pm$Mo, Ta) were carried by early exsolved and expelled aqueous fluids. The first evidence of element enrichment is recorded at distances of 4–5 times the thickness of the dykes, with exponentially increasing gains of those fluid-mobile elements proximal to the pegmatite margin. Enrichments that were detected farthest from the pegmatite margins were those of Li and Cs, followed by Rb and, to a lesser extent, Sn, F, B, Be, and Tl. The most evolved (fractionated) aplite-pegmatites generated the broadest haloes, with concentrations higher than 200 ppm Li, 30 ppm Cs, 300 ppm Rb, and 15 ppm Sn in the metasediments indicating proximity to a mineralized dyke. In addition, absolute gains of up to ~4000 ppm Li, ~1300 ppm Cs, ~1300 ppm Rb, and 170 ppm Sn in the host rocks could point to the presence of superimposed haloes from multiple evolved dykes.

1. Introduction

Raw materials that are of great economic and strategic relevance, principally due to their use in green technologies, are described as 'critical' (Blengini et al., 2020). In the last decade, lithium has become one of the main critical raw materials, due to significant increases in global demand because of its use in rechargeable batteries for electric vehicles (Jaskula, 2017; Gourcerol et al., 2019; Bibienne et al., 2020). Subsequently, geological resource exploration has been focused on the discovery of new Li-deposits and/or the re-assessment of known

---

reservoirs (Kesler et al., 2012; Gourcerol et al., 2019; Pesquera et al., 2020). Among these deposits, granitic pegmatites represent an important source of not only Li, but also Sn, Ta, Nb, Be, Cs, Rb, Sc, Th, U and rare earth elements (REE) (Černý and Ercit, 2005; Selway et al., 2005; Linnen et al., 2012; London, 2018; Roda-Robles et al., 2018; Zhang et al., 2021). Granitic pegmatites are divided into two main families that differ in terms of their trace element signature, namely LCT and NYF, with the most evolved examples being enriched in Li-Cs-Ta (±Rb, Be, Sn, B, P and F), and Nb-Y-F (±Be, REE, Sc, Ti, Zr, Th and U), respectively (Černý and Ercit, 2005).

With greater emphasis on sustainable mineral exploration in recent years, many research projects have proposed innovative and less-invasive mineral exploration techniques that allow reduction of the environmental footprint (Cardoso-Fernandes et al., 2019, 2020; Kesselring et al., 2020; Ruiz-Coupeau et al., 2020; Xing et al., 2021; Müller et al., 2022). Since sustainability factors seem to be mainly achievable during the early stages of the natural resource extraction process, a complete understanding of the mineralization itself, and its effects on surrounding rocks, can contribute to sustainable mineral exploration (Kesselring et al., 2020; Pell et al., 2021).

The intrusion and evolution of granitic–pegmatitic melts often results in the alteration of surrounding rocks and the development of metasomatic aureoles ('metasomatic aureole' or 'geochemical halo' are used synonymously throughout this work) (Shearer et al., 1984; London, 1986; Morgan and London, 1987; Lentz and Gregoire, 1995; Selway et al., 2005; Teng et al., 2006; Estrade et al., 2015; Pérez-Soba and Villaseca, 2019). This type of contact metasomatism originates from the influx of pegmatite-derived fluids, commonly during late- to post-magmatic stages of the intrusion, causing a compositional change of pre-existing minerals and crystallization of new phases in the exocontact (Morgan and London, 1987; London, 1986; Kretz et al., 1989; Selway et al., 2005; Migdisov and Williams-Jones, 2014; Fuchsloch et al., 2019; Barros et al., 2020). The evolution of this geochemical alteration depends on 1) crustal temperature and pressure conditions (related to the structural relationship between the pegmatite and host rocks); 2) the composition of host-rocks, pegmatitic melt and related fluids; and 3) the fluid/rock ratio (Audétat et al., 2008; Beinlich et al. 2010; Thomas and Davidson, 2012; Thomas and Davidson, 2016). Recent studies have shown that the transition from a pure magmatic to a pure hydrothermal environment during pegmatite crystallization is a complex multi-stage process (Kaeter et al., 2018; Ballouard et al., 2020; Barros et al., 2020; Hulsbosch and Muchez, 2020; Shaw et al., 2022). Paragenetic studies indicate that, according to internal pegmatite evolution, melt–melt–fluid immiscibility occurs during this transition, where at least three immiscible phases can coexist (e.g., Veksler, 2004; Kaeter et al., 2018; Ballouard et al., 2020; Barros et al., 2020; Hulsbosch and Muchez, 2020; Shaw et al., 2022). Aqueous fluids gradually become the prevailing phase over hydrosaline melts as cooling of the pegmatitic melt proceeds, which causes variations in the capacities of such melts–fluids to leach and transport different metals (e.g., Ballouard et al., 2020). The aqueous phases mainly consist on H_2O, CO_2, and chloride salts (predominantly NaCl), and their compositions are controlled by the nature of the related magma, whereas the exsolution of immiscible fluids is controlled by pressure (London, 1986; Audétat et al., 2008; Thomas et al., 2012; Audétat, 2019). These processes become more complex when other volatiles such as B, F and P (and alkali elements such as Li), intervene in the system, lowering the solidus temperature and magma viscosity (London, 1987; Pollard et al., 1987; Thomas et al. 2000; Raith et al., 2004; Bartels et al., 2011; Thomas et al., 2012). In addition to their role as fluxing components, B and F can act as important ligands to form complexes with metals that could be transported from the pegmatite to the surrounding host rocks during fluid exsolution (London, 1987; Morgan and London, 1987; Pollard et al., 1987; Thomas et al., 2000, 2003; Migdisov and Williams-Jones, 2014).

Mass transfer in metasomatic systems is reflected in whole-rock elemental gains and losses, which vary depending on the chemical behavior of elements under specific P-T-X conditions (Gresens, 1967; Grant, 1986; Ague, 1994; Lentz and Gregoire, 1995). The distance from a pegmatite intrusion where gains of fluid-mobile elements are observed defines the metasomatic aureole—its width partly controlled by the factors mentioned above—but also by the size of the intrusion (Morgan and London, 1987; Galeschuk and Vanstone, 2007). In the case of LCT pegmatites, adjacent metasomatic aureoles are characterized by an enrichment in elements such as Li, Cs, and Rb, and metal anomalies can extend >150 m beyond the contact between the pegmatites and their country rocks (Černý, 1989; Selway et al., 2005; Galeschuk and Vanstone, 2007; Linnen et al., 2012; Martins et al., 2017). According to pioneering works of Trueman (1978), Shearer et al. (1986), Morgan and London (1987) and Černý (1989), Li-rich aureoles tend to be broader than those of Rb and Cs, and these geochemical haloes are broader in metasedimentary host rocks compared to those observed in igneous or meta-igneous rocks. More recent studies have revealed that W, In and Sn anomalies in host rocks may also be good indicator of nearby LCT pegmatites (e.g., Galeschuk and Vanstone, 2007). Accordingly, the systematic lithogeochemical study of country rocks in pegmatite fields is a useful and small-footprint exploration tool to identify buried pegmatites with economic potential (e.g., Selway et al., 2005; Martins et al., 2017).

Abundant Li-pegmatites crop out in the Iberian Massif throughout a 500 km-long and NW–SE striking belt, comprising different pegmatite fields that have been exploited from the 1920s (Fuertes-Fuente and Martin-Izard, 1998; Charoy et al., 2001; Neiva and Ramos, 2010; Vieira et al., 2011; Neiva et al., 2012; Martins et al., 2012; Antunes et al., 2013; Roda-Robles et al., 2016, 2018; Garate-Olave et al., 2017, 2020; Roza-Llera et al., 2019). These pegmatites constitute a metallogenetic province of the Variscan Orogeny. Geochemical, geochronological, and structural data suggest that they are related to the main episode of granitic magmatism between 330 and 290 Ma (Roda-Robles et al., 2016, 2018 and references therein). The Iberian pegmatites are characterized by: (1) complex layering and textural variations (aplitic, pegmatitic and/or aplitic + pegmatitic); (2) an enrichment in Li (±F, Sn, P, Nb, Ta, Rb and Cs); (3) an overall absence of quartz cores, internal concentric zoning or graphic intergrowths; and, (4) the occurrence of spodumene, petalite, Li-micas/lepidolite and/or amblygonite group minerals as the main Li-bearing minerals (Roda-Robles et al., 2016, 2018). The Fregeneda–Almendra Pegmatite Field is one of the main pegmatite fields of the Iberian Massif, which has been thoroughly studied in terms of mineralogy and crystallochemistry, petrogenesis, and exploration techniques (López-Plaza et al., 1982; Roda-Robles et al., 1995, 1996, 1999, 2010; Vieira et al., 2011; Cardoso-Fernandes et al., 2019; Cardoso-Fernandes et al., 2020).

The main goal of this contribution is to characterize metasomatic processes and related geochemical modifications associated with the intrusion of aplite-pegmatites into pelitic and psammitic metasediments within the Fregeneda–Almendra Pegmatite Field. We present a prospect-scale study which relies on whole-rock geochemistry and mass-balance equations to evaluate metasomatic processes associated with four representative aplite-pegmatite bodies. The selected localities that were examined are the Feli open pit (Li-mica-bearing pegmatite), the Alberto open pit (spodumene-bearing pegmatite), the Hinojosa–Saucelle road (petalite-bearing pegmatite) and the Tumbo de la Caldera area (intermediate pegmatite).

2. Geological setting

The Fregeneda–Almendra Pegmatite Field is located in the Central Iberian Zone (CIZ) of the Iberian Massif, south of the allochthonous terranes of the Galicia–Trás-os-Montes Zone (Martínez Catalán et al., 2014, 2021 and references therein; Fig. 1a and b). Located SW of the Tormes Dome, this pegmatite field occurs along a ~30 km-long and ~7 km-wide W–E belt of Neoproterozoic to Cambrian metasediments delimited to the N by the Paleozoic successions of the Poiares Synform
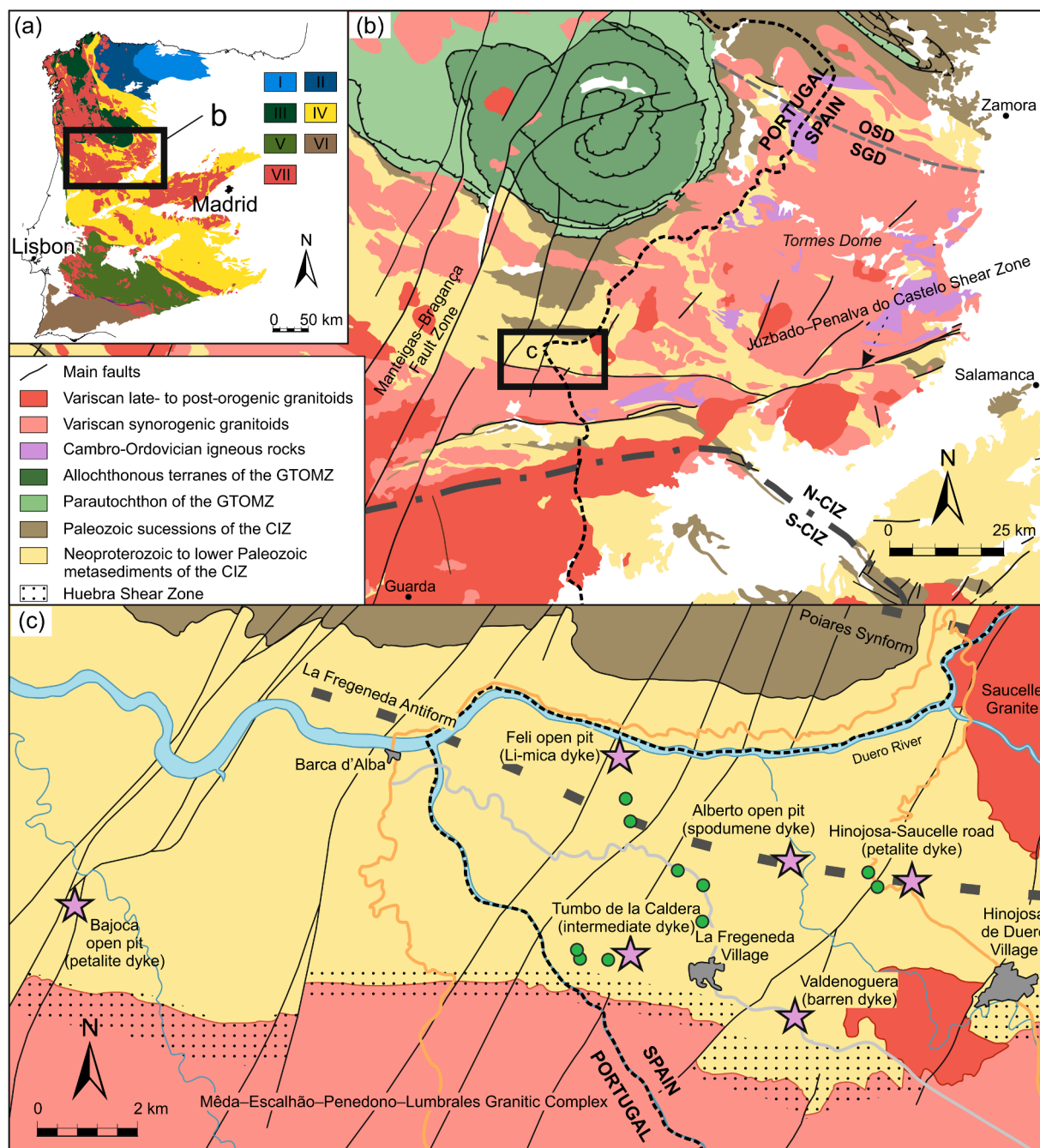
Fig. 1. (a) Geological map of the Iberian Massif, subdivision based on Julivert et al. (1972) and Variscan granitoids adapted from Rodríguez Fernández and Oliveira (2015). I: Cantabrian Zone, II: West Asturian-Leonese Zone, III: Galicia-Trás-os-Montes Zone (GTOMZ), IV: Central Iberian Zone (CIZ), V: Ossa-Morena Zone, VI: South Portuguese Zone, VII Variscan granitoids. (b) Regional geological map based on Rodríguez Fernández and Oliveira (2015), with subdivision of the Ollo de Sapo Domain (OSD) and Schist-Greywacke Domain (SGD), and distinction of the Northern Central Iberian Zone (*N*-CIZ) and Southern Central Iberian Zone (S-CIZ; Talavera et al., 2012; Villaseca et al., 2014). (c) Detailed geological map of the Fregeneda–Almendra Pegmatite Field, displaying the location of studied dykes (stars) and control samples (green dots). Geologic units based on Silva and Ribeiro (1994) and Rodríguez Fernández et al. (2000).

(Armorican Quartzite Formation), to the S by the Mêda–Escalhão–Penedono–Lumbrales (MEPL) Granitic Complex, to the E–NE by the Saucelle Granite, and to the W by the Vilariça Segment of the Manteigas–Bragança Fault Zone (Roda-Robles et al., 1999, 2010, 2016; Vieira et al., 2011; Díez Fernández and Pereira, 2016; López-Moro et al., 2018; Cardoso-Fernandes et al., 2019; Ferreira et al., 2019, 2020; Fig. 1b and c).

2.1. Stratigraphy, structure and metamorphism

The metasedimentary belt that hosts the Fregeneda–Almendra Pegmatite Field is constituted mainly by a thick Neoproterozoic to lower Paleozoic terrigenous sequence included in the Douro Group of Sousa (1982). As other pre-Ordovician metasediments of the CIZ, the Douro Group represents turbiditic flysch deposits from the northern continental margin of Gondwana (Silva and Ribeiro 1994; Rodríguez Fernández et al., 2000; Valladares et al., 2002; Gutiérrez-Alonso et al., 2003; Rodríguez-Alonso et al., 2004; Ugidos et al., 2010; Talavera et al.,

2012; Villaseca et al., 2014). This thick pile of pelitic and psammitic metasediments is characterized in the region by millimeter- to centimeter-scale alternations of phyllites (±lutites, slates, schists) and greywackes, with interbedded quartzite and calcsilicate layers (Silva and Ribeiro 1994; Rodríguez Fernández et al., 2000). Because the studied area has been traditionally included in the southern Schist Greywacke Domain of the CIZ according to stratigraphic evidence, the pre-Ordovician metasediments of the area have been included within the Schist–Greywacke Complex (Carrington da Costa, 1950; Silva and Ribeiro 1994; Rodríguez Fernández et al., 2000; Teixeira et al., 2011; Talavera et al., 2012). Villaseca et al. (2014) proposed an alternative subdivision of the CIZ based on geochemical evidence. According to these authors, the studied aplite-pegmatite dykes would have intruded Neoproterozoic to lower Paleozoic metasediments of the northern CIZ (*N*-CIZ) that chemically differ slightly from those of the Schist–Greywacke Complex *sensu stricto*, which would be restricted to the southern CIZ (S-CIZ; Fig. 1b).

The Neoproterozoic to lower Paleozoic metasediments of the studied area recorded a Variscan polyphasic deformation and metamorphism (Escuder Viruete et al., 1994; Silva and Ribeiro, 1994; Rodríguez Fernández et al., 2000; Dias da Silva et al. 2017). The first deformation phase (D_1), related to crustal thickening, was accompanied by a low-grade Barrovian-type metamorphism (M_1) with peak conditions in the greenschist facies (Díez Fernández and Pereira, 2016; Dias da Silva et al., 2017). The M_1 metamorphic grade decreases to the west, with wide areas belonging to the biotite zone and minor ones to the chlorite zone (Silva and Ribeiro, 1994; Rodríguez Fernández et al., 2000; Díez Fernández and Pereira, 2016; Dias da Silva et al., 2017). Coeval with the exhumation of high-grade metamorphic domains during the orogenic collapse (D_2), the associated high temperature-low pressure metamorphism (M_2) resulted in the generation of gneisses and migmatites. These high-grade rocks occur only in close proximity to some granitic intrusions, showing a sharp transition to the main low-grade domain (Díez Fernández and Pereira, 2016; Dias da Silva et al., 2017). In addition, the intrusion of some syn- and late- to post-D_3 Variscan granites generated narrow contact metamorphism aureoles that locally overprint the regional metamorphism (Rodríguez Fernández et al., 2000; Díez Fernández and Pereira, 2016; Dias da Silva et al., 2017). The main structures in the Fregeneda–Almendra area are WNW–ESE striking and NE vergent antiforms and synforms, which have been related to the D_1 deformation phase of the region and appear to be associated with an S_1 slaty-cleavage (Escuder Viruete et al., 1994; Silva and Ribeiro 1994; Rodríguez Fernández et al., 2000; Dias da Silva, 2014; Fig. 1c). After the second deformation phase (D_2), a ductile strike-slip deformation phase (D_3) took place during *retro*-metamorphism (M_3) in the region, which led to the development of upright D_3 folds (e.g., Díez Fernández and Pereira, 2016; Díez Fernández and Pereira, 2017). Late-Variscan tectonic features in the study area include NE–SW to NNE–SSW faults that cross-cut previous W–E striking shear zones such as the large-scale (D_3) Juzbado–Penalva do Castelo Shear Zone (Silva and Ribeiro 1994; Rodríguez Fernández et al., 2000; Díez Fernández and Pereira, 2016; Dias da Silva et al., 2017; Fig. 1b and c).

2.2. Variscan granitic magmatism

Leaving aside minor Cambro–Ordovician crust-derived peraluminous magmatic rocks (Bea et al., 2007; Villaseca et al., 2016; García-Arias et al., 2018), the main magmatic event in the area, by far, corresponds to the widespread emplacement of Variscan granitic intrusions (Dias et al., 1998; López-Moro and López-Plaza, 2004; Valle-Aguado et al., 2005; Gutiérrez-Alonso et al., 2011; Teixeira et al., 2011, 2012; Díez Fernández and Pereira, 2016; López-Moro et al., 2017; Pereira et al., 2018; Ferreira et al., 2019, 2020; Fig. 1b and c). These granitic intrusions have been traditionally classified considering their temporal relationship with respect to the Variscan orogenic stages, distinguishing syn- and late- to post-D_3 intrusions. Consequently, the MEPL Granitic Complex (~319–313 Ma; U–Pb in zircon) has been defined as *syn*-D_3, and the Saucelle Granite as late- to post-orogenic (Rodríguez Fernández et al., 2000; Díez Fernández and Pereira, 2016; Pereira et al., 2018; Ferreira et al., 2019; Fig. 1b and c). The MEPL Granitic Complex consists mainly of coarse- to medium-grained two-mica peraluminous granites and biotite-rich porphyritic monzogranites, while the Saucelle Granite is composed of homogeneous undeformed peraluminous two-mica leucogranites (Rodríguez Fernández et al., 2000; Díez Fernández and Pereira, 2016; Pereira et al., 2018; Ferreira et al., 2019, 2020).

2.3. Geology of the aplite-pegmatites from Fregeneda–Almendra

Hundreds of pegmatite bodies have been identified in the Fregeneda–Almendra Pegmatite Field, which have been classified into eleven types according to their mineralogy, textural features, shape and size, degree of fractionation, and relationships with deformation and tectonic structures (e.g., Roda-Robles et al., 1999, 2010; Vieira et al., 2011). Overall, the aplite-pegmatites of Fregeneda–Almendra display a regional spatial zonation from barren to evolved types with increasing distance from the MEPL Granitic Complex, as demonstrated by the northward-increasing Li-F contents (Roda-Robles et al., 1996, 1999, Vieira et al., 2011). Of the eleven recognized pegmatite types (Table 1), four consist of concordant barren dykes that occur relatively close or within the MEPL Granitic Complex, with quartz, K-feldspar > albite, muscovite, tourmaline ± andalusite ± garnet (types 1 to 4). The remaining seven pegmatite types consist of discordant dykes with a N10°–50°E strike. Intermediate (in terms of fractionation) bodies (types 5 and 6) are characterized by the occurrence of Fe–Mn phosphates, amblygonite group minerals ± tourmaline, and micas and feldspars showing higher Rb and Cs contents relative to the concordant barren aplite-pegmatites. Evolved aplite-pegmatites of the Fregeneda–Almendra field host spodumene, petalite, Li-micas and amblygonite group minerals, with significant enrichment in Li ± F, Sn, Rb, Nb > Ta, B, P and Be (types 7 to 10; Table 1). Finally, type 11 dykes are represented by quartz veins rich in cassiterite, micas, and albite. According to Vieira et al. (2011), pegmatites of Fregeneda–Almendra do not relate to the fractional crystallization of a single magma, and their possible petrogenetic linkage with the MEPL Granitic Complex is not completely understood.

3. Materials and methods

3.1. Sampling

A total of 71 rock samples were collected for the present study: four from representative subvertical discordant aplite-pegmatites (types 6 to 9; Table 1) (8–12 Kg/sample), 44 from their host rocks (variably metasomatized), four from host metasediments of a type 3 concordant barren dyke, and fourteen metasedimentary 'control samples' representing non-metasomatized samples (2–3 Kg/sample for the control samples and ~1 Kg/sample for the rest) (Table 2). Control samples were collected from country rocks surrounding the selected dykes (>300 m away), attempting to avoid any possible effect related to the intrusion of the aplite-pegmatites. At five of the localities with favourable outcropping conditions (Feli open pit, Alberto open pit, Hinojosa–Saucelle road, Tumbo de la Caldera, and Valdenoguera; Fig. 1c), a systematic sampling was performed, where all samples were collected in a section perpendicular to the strike of the dykes and georeferenced (Table 2). The ideal length of the profiles for the halo sampling was about 10 times the width of the intrusive body, with a progressive increase of the number of collected samples close to the dyke (following procedures of the H2020 GREENPEG project). Additionally, five drill core samples from the Bajoca open pit (pegmatite type 7) were also included (Table 2). In total, 60 thin sections were selected for the petrographic study.

Table 1
Summary of main features for the distinguished pegmatite types in the Fregeneda-Almendra Pegmatite Field.

Type	Mineralogy		Morphology and structure	Remarks		Enrichment
	Main	Other				
[1]	Qz, Kfs	Ms, Ab, Tur	elongated bodies; thickness < 50 cm	scarce; intragranitic (MEPL)		K, Al, (B, P)
[2]	Qz, And	Ms, Tur, Kfs	concordant dykes; deformed; unzoned; thickness < 50 cm	scarce; boudinaged		Al, Si, (B, K)
[3]	Qz, Kfs, Ms, Ab, Tur	And, Grt, Bt, Ap	concordant dykes; deformed; locally with internal zoning; thickness < 1 m	abundant; graphic texture; Valdenoguera*		Al, Na, B
[4]	Qz, Kfs, Ms	Ab, Tur, Bt	Irregular masses or lenticular forms; unzoned	more common to the east; graphic texture		K, Al, (B, P)
[5]	Kfs	Qz, Ms, Py	discordant dykes; NNE–SSW; thickness > 1 m	scarce; main component pink Kfs		K
[6]	Qz, Kfs, Ab, Ms	Fe-Mn Pho, Mbs, Tur, Clb-Ttl	discordant dykes; NNE–SSW; thickness 10 cm to 2 m	most abundant; internal layering usual; Tumbo de la Caldera*		Na, K, Al, (P, Li)
[7]	Qz, Ab, Ptl	Ms, Mbs, Cst, Clb-Ttl, Ecp	discordant dykes (NNE–SSW) without internal zoning; thickness 5–30 m	main intrusions: Bajoca* and Hinojosa de Duero*		Li, P, (Sn)
[8]	Qz, Ab, Spd, Kfs	Ms, Ptl, Mbs, Cst, Clb-Ttl	discordant dykes (NNE–SSW) without internal zoning; thickness 4–15 m	main intrusion: Alberto*		Li, P, (Sn)
[9]	Qz, Ab, Kfs, Li-mica, Ms, Spd	Ms, Cst, Mbs, Clb-Ttl	discordant dykes (NNE–SSW) with internal zoning common; thick. < 15 m	main intrusion: Feli*		Li, Sn, P, F, (Rb, Cs)
[10]	Qz, Ab, Li-mica, Kfs	Ms, Cst, Mbs, Clb-Ttl,	discordant dykes (NNE–SSW); internal zoning common; thick. < 3 m	main intrusions: Cármen, Riba d'Alva and Ramalha		Li, Sn, P, F, (Rb, Cs)
[11]	Qz, Cst, Ms	Ab, Kfs, Ap, Clb-Ttl	discordant veins; deformed; thickness < 50 cm	hydrothermal veins		Sn, Si, K, (P)

Table modified from Roda-Robles et al. (1996, 1999, 2010) and Vieira et al. (2011). Pho: phosphate; Mbs: montebrasite; Clb: columbite; Ttl: tantalite; Ecp: eucryptite. Other mineral abbreviations from Whitney and Evans (2010).
Types 1 to 4: barren dykes; types 5 and 6: intermediate dykes; types 7 to 10: evolved dykes; type 11: hydrothermal veins.
* Selected localities for this study.

3.2. Whole-rock analyses

All samples were sent to Activation Laboratories Ltd. (Ancaster, Ontario, Canada) for whole-rock major and trace element analyses (complete results in Supplementary Table 1). Pegmatite samples were crushed to a nominal grain size of 1 cm at the Geology Department of the University of the Basque Country and then the resultant material was split to obtain representative sub-samples of 500 g. In the case of host metasediments, samples were cut to obtain representative sub-samples of 300 g. Each sample was then crushed up to 80 % (passing 2 mm), split using a riffle splitter (250 g), and pulverized up to 95 % (passing 105 μm) using a mild steel pulverizer. Major and trace element concentrations were obtained by different analytical techniques, which are listed together with respective detection limits in Supplementary Table 1. To obtain major element (SiO_2, TiO_2, Al_2O_3, $Fe_2O_3^t$, MnO, MgO, CaO, Na_2O, K_2O, P_2O_5) and Zr, Sc, Hf and Lu concentrations, a lithium metaborate/tetraborate fusion was performed to dissolve the entire sample. Major elements were measured using X-ray fluorescence whereas Sc and Zr were analyzed by inductively coupled plasma – optical emission spectrometry (ICP-OES) and Hf and Lu by inductively coupled plasma – mass spectrometry (ICP-MS). Other trace element concentrations were measured by ICP-MS, but with a previous sodium peroxide fusion. Fluorine concentrations were analyzed by ion selective electrode (ISE) following a lithium borate fusion and dissolution in dilute nitric acid.

4. Field description and petrography

4.1. Aplite-pegmatite dykes

The pegmatitic bodies selected for the study of metasomatism related to the Fregeneda–Almendra Pegmatite Field correspond to barren (Valdenoguera [type 3]), intermediate (Tumbo de la Caldera [type 6]), petalite-bearing (Hinojosa–Saucelle road [type 7]), spodumene-bearing (Alberto open pit [type 8]), and Li-mica-bearing (Feli open pit [type 9]) aplite-pegmatite dykes (Tables 1 and 2; Fig. 1c). Excluding the sub-horizontal concordant E–W trending dyke from Valdenoguera, the aplite-pegmatite bodies are subvertical dykes with a NNE–SSW strike that crosscut the regional foliation of the host rocks (Fig. 2a). These dykes are characterized by variable thicknesses from 1.2 to 7.0 m

(Table 2), and a marked variation in grain size, from few millimeters up to several centimeters. A layering, parallel to the contact with the host rock, is observed in the case of the Feli open pit, but neither internal zoning nor a quartz core are observed. The complementary samples from the Bajoca open pit are from a drill core that cuts two subvertical petalite-bearing pegmatite dykes where no layering is observed. A notable feature of the studied aplite-pegmatites is the abundance of unidirectional solidification textures (UST) such as comb crystals of feldspars, spodumene, petalite and tourmaline (depending on the pegmatite-type) across the entire width of the dykes (Fig. 2b).

The barren concordant dyke from the Valdenoguera area mainly consists of quartz, K-feldspar, albite, muscovite and minor tourmaline, with accessory garnet, andalusite, and biotite. Likewise, main minerals for the Tumbo de la Caldera intermediate discordant dyke are quartz, albite, K-feldspar and muscovite, with accessory Fe–Mn phosphates, montebrasite, tourmaline, cassiterite, and columbite group minerals. The Hinojosa–Saucelle and Bajoca dykes are mainly composed of quartz, petalite, albite, and K-feldspar, along with minor muscovite and cassiterite, and accessory Fe–Mn phosphates, montebrasite, and eucryptite. Similarly, the studied dyke from Alberto is composed of quartz, spodumene, albite, K-feldspar and muscovite, with subordinate petalite and trace montebrasite and Fe–Mn phosphates. Minerals comprising the studied intrusion at Feli are quartz, albite, K-feldspar, Li-muscovite, muscovite; minor spodumene; and accessory montebrasite, cassiterite, columbite group minerals, apatite, eucryptite, and Fe–Mn phosphates.

Apart from the primary mineralogy described above, a variety of textures and secondary mineral assemblages were observed in the aplite-pegmatites that could represent manifestations of late- to post-magmatic processes (Fig. 2c–f and Fig. 3). Specific evidence of Na-metasomatism includes: (i) subsolidus growth of irregular patchy perthites inside some K-feldspar crystals; (ii) presence of 'chessboard' albite and saccharoidal pure albite (Fig. 2c and d); (iii) common occurrence of myrmekitic quartz blebs inside pure albite; (iv) relative abundance of high temperature secondary Na-Fe-Mn-phosphates, mainly belonging to the alluaudite group, replacing primary Fe-Mn phosphates (see Roda-Robles et al., 2010); and, (v) presence of late apatite and other Ca-rich phosphates (e.g. messelite, crandallite), whose requisite Ca is derived from plagioclase during albitization. All of these textures are observable in pegmatite types 6 to 9 of Fregeneda–Almendra, mainly in the most evolved pegmatitic intrusions. Evidence of greisenization is less

Table 2
Summary of the sampling performed for the present study.

N°	Locality	UTM coordinates (X;Y, sheet 29 T, datum ETRS89)	Sample	Lithology	Subtype	Related dyke-type (thickness)	Distance from the dyke (m)
1	Feli	677620; 4543771	FR-43	Psammitic and pelitic metasediment	Metasomatized	Li-mica (1.8 m)	0 E
2	Feli	677620; 4543771	FR-44				0.5 E
3	Feli	677621; 4543770	FR-45				1 E
4	Feli	677622; 4543770	FR-46				2.5 E
5	Feli	677624; 4543768	FR-47				5 E
6	Feli	677628; 4543765	FR-48				10 E
7	Feli	677618; 4543772	FR-49				0 W
8	Feli	677616; 4543773	FR-50				0.5 W
9	Feli	677616; 4543774	FR-51				1 W
10	Feli	677615; 4543774	FR-52				1.8 W
11	Alberto	681111; 4542020	F-38	Psammitic and pelitic metasediment	Metasomatized	Spodumene (2.6 m)	0 SE
12	Alberto	681111; 4542020	F-39				0.5 SE
13	Alberto	681112; 4542020	F-40				1 SE
14	Alberto	681113; 4542019	F-41				2.5 SE
15	Alberto	681114; 4542018	F-42				5 SE
16	Alberto	681108; 4542022	F-43				0 NW
17	Alberto	681107; 4542022	F-44				0.5 NW
18	Alberto	681107; 4542023	F-45				1 NW
19	Alberto	681106; 4542023	F-46				2.5 NW
20	Alberto	681105; 4542024	F-47				5 NW
21	Hinojosa-Saucelle	683500; 4541515	FR-18	Psammitic and pelitic metasediment	Metasomatized	Petalite (7 m)	0 E
22	Hinojosa-Saucelle	683501; 4541515	FR-19				0.5 E
23	Hinojosa-Saucelle	683502; 4541516	FR-20				1 E
24	Hinojosa-Saucelle	683503; 4541517	FR-21				2 E
25	Hinojosa-Saucelle	683504; 4541516	FR-22				3 E
26	Hinojosa-Saucelle	683507; 4541516	FR-23				6 E
27	Hinojosa-Saucelle	683513; 4541516	FR-24				12 E
28	Hinojosa-Saucelle	683521; 4541515	FR-25				20 E
29	Hinojosa-Saucelle	683535; 4541511	FR-26				35 E
30	Hinojosa-Saucelle	683493; 4541513	FR-27				0 W
31	Hinojosa-Saucelle	683492; 4541515	FR-28				0.5 W
32	Hinojosa-Saucelle	683492; 4541513	FR-29				1 W
33	Hinojosa-Saucelle	683491; 4541514	FR-30				2 W
34	Hinojosa-Saucelle	683490; 4541514	FR-31				3 W
35	Hinojosa-Saucelle	683487; 4541513	FR-32				6 W
36	Hinojosa-Saucelle	683482; 4541511	FR-33				12 W
37	Hinojosa-Saucelle	683473; 4541507	FR-34				20 W
38	Tumbo de la Caldera	678015; 4539988	BAR-07	Psammitic and pelitic metasediment	Metasomatized	Intermediate (1.2 m)	0 W
39	Tumbo de la Caldera	678014; 4539988	BAR-08				1 W
40	Tumbo de la Caldera	678012; 4539988	BAR-09				2.5 W
41	Tumbo de la Caldera	678010; 4539988	BAR-10				5 W
44	Tumbo de la Caldera	678017; 4539988	BAR-13				0 E
45	Tumbo de la Caldera	678017; 4539988	BAR-14				0.5 E
46	Tumbo de la Caldera	678018; 4539988	BAR-15				1 E
47	Bajoca	666804; 4540779	BJ04-B-DD	Psammitic and pelitic metasediment	Metasomatized	Petalite (4.75 m)	0.5 down
48	Bajoca	666804; 4540779	BJ04-C-DD			Petalite (6.2 m)	10 up
49	Bajoca	666804; 4540779	BJ04-D-DD				0 up
50	Bajoca	666804; 4540779	BJ04-E-DD				0 down
51	Bajoca	666804; 4540779	BJ04-F-DD				5 down
52	Valdenoguera	681146; 4538892	T4-19–01	Psammitic and pelitic metasediment	Metasomatized	Barren (1.2 m)	0 down
53	Valdenoguera	681146; 4538892	T4-19–02				0.5 down
54	Valdenoguera	681146; 4538892	T4-19–03				1 down
55	Valdenoguera	681146; 4538892	T4-19–04				2 down
N°	Locality	UTM coordinates (X;Y, sheet 29 T, datum ETRS89)	Sample	Lithology	Subtype	Related dyke-type (thickness)	Distance from the dyke (m)
56	Alberto	679250; 4541464	Ctrl_01	Psammitic and pelitic metasediment	Control sample	–	–
57	Feli	677643; 4543119	Ctrl_02				
58	Feli	677695; 4542679	Ctrl_03				
42	Tumbo de la Caldera	678004; 4539987	Ctrl_04				

Table 2 (*continued*)

N°	Locality	UTM coordinates (X;Y, sheet 29 T, datum ETRS89)	Sample	Lithology	Subtype	Related dyke-type (thickness)	Distance from the dyke (m)
43	Tumbo de la Caldera	677998; 4539984	Ctrl_05				
59	Hinojosa-Saucelle	690967; 4539994	Ctrl_06				
60	Hinojosa-Saucelle	657305; 4546444	Ctrl_07				
61	Alberto	679507; 4540642	Ctrl_08	Psammitic and pelitic metasediment	Control sample	–	–
62	Feli	679046; 4541657	Ctrl_09				
63	Hinojosa-Saucelle	683023; 4541418	Ctrl_10				
64	Hinojosa-Saucelle	683051; 4541428	Ctrl_11				
65	Tumbo de la Caldera	677959; 4539973	Ctrl_12				
66	Tumbo de la Caldera	676965; 4539987	Ctrl_13				
67	Tumbo de la Caldera	676962; 4540028	Ctrl_14				
68	Feli	677619; 4543772	FEL-02	Aplite-pegmatite	Li-mica	–	–
69	Alberto	681110; 4542021	ALB-01		Spodumene		
70	Hinojosa-Saucelle	683499; 4541514	PET-01		Petalite		
71	Tumbo de la Caldera	678016; 4539988	BAR-06		Intermediate		

Samples from Bajoca are from a drill core that cuts two dykes. In that case, "up" and "down" mean the relative location of the samples regarding the related dyke within the drill core.

prevalent. Limited development of small (<50 cm) irregular greisen masses, comprised of equigranular fine-grained aggregates of quartz and white(-greenish-pinkish) micas, occur in spodumene- and Li-mica-bearing pegmatites, particularly in the latter (Fig. 2e). Spodumene may be primary or may occur as a secondary phase replacing petalite and forming spodumene-quartz intergrowths (SQI) (Fig. 2f), and it can also be altered to secondary white micas. Columbite group minerals also show textures that are indicative of late-stage dissolution and recrystallization of oxides. Secondary sericite is also present, replacing both K- and Na-feldspars, and differs in texture and crystal-size from a secondary interstitial (greenish) gilbertite observed in some samples. Locally, massive aggregates of fine-grained eucryptite and/or cookeite replace spodumene and petalite in type 8 pegmatites. The timing of cookeite formation seems coeval with that of sericite, representing the latest mineral phases of the studied intrusions (Fig. 3).

4.2. Host metasediments

The host rocks of the selected aplite-pegmatite dykes are part of a monotonous siliciclastic metasedimentary sequence with turbiditic features. This series comprises a roughly rhythmic alternation (millimetric to centimetric) of pelites and psammites (Fig. 4a) with minor calc-silicate rocks and no volcanic sequences. Overall, the studied psammitic and pelitic metasediments are fine-grained, and they preserve sedimentary structures such as erosion surfaces, parallel lamination, ripples, load casts, and graded bedding (Fig. 4b). These features are mainly visible in the most psammitic layers. Fresh metapelite samples are grey to dark-grey, with slight green–blue–violet tints, which contrast with the light-colored psammitic layers (Fig. 4b).

The metasediments have granolepidoblastic texture (Fig. 4c and d). In the more pelitic layers, the metamorphic overprint is visible, with randomly oriented porphyroblasts of biotite and a well-developed slaty-cleavage oblique to the sedimentary laminations (Fig. 4c and d). These metasediments are comprised of quartz, biotite, and muscovite in variable amounts, plus accessory plagioclase (±K-feldspar), apatite, zircon, and oxides (Fig. 4c and d). In general, the mineralogy of the selected samples is fairly homogeneous, but in some thin sections in which later modifications are perceived, the occurrence of tourmaline or chlorite (±calcite, ± epidote, ± titanite) is common.

In some of the metasedimentary samples a pseudomorphic replacement of biotite by chlorite is observed. At outcrop scale, the distribution of these samples is heterogeneous, representing local alteration processes that are often related to fractures, but independent from the pegmatite dykes. In thin section, the degree of chloritization is also variable, with some samples displaying relatively weak alteration that contrasts with the pervasive replacement observed in others (Fig. 4e and f). When chloritization is not significantly developed in the sample, the replacement by chlorite commonly evolves along microcracks, and biotite crystals remain unaffected within a few μm of these microfractures (Fig. 4e). In the less altered samples, chlorite partially replaces only some small biotite flakes, whereas in the case of strongly chloritized samples only occasional moderately larger biotite crystals remain unaltered (Fig. 4e and f).

A conspicuous feature observed in samples close to the selected dykes is the abundance of tourmaline-rich layers (Fig. 5). Tourmaline in these samples has a euhedral to subhedral prismatic habit, and commonly appears parallelly-arranged, with the C-axis following the S_1 slaty-cleavage (Fig. 5a). The occurrence of tourmaline is strongly controlled by the S_0 sedimentary fine-scale layering, with tourmaline-rich laminae present in the pelitic layers and tourmaline-poor or -absent areas corresponding to more psammitic layers (Fig. 5b). In some samples tourmaline displays a pronounced, gradational to discontinuous optical zoning (with blue-green-grey cores and brown-red rims), whereas others, containing brown to reddish tourmaline, slight or no optical zoning is observed. Overall, tourmaline crystals show a strongly colored to almost colorless pleochroism, and contain numerous inclusions of other minerals. The abundance of tourmaline decreases gradually as the distance from the pegmatite increases (Fig. 5c–f). Nearly pure tourmalinite layers are present in some of the samples collected within a few centimeters of the pegmatites (composed almost exclusively of tourmaline, up to 90 % in vol.; Fig. 5c). Tourmaline crystal-size also correlates inversely with distance from the pegmatite, with euhedral prisms of up to 2 mm found at the pegmatite contact and disseminated subhedral crystals of <0.1 mm in distal samples where tourmaline represents an accessory phase (Fig. 4d and Fig. 5a).

Pale beige-brown micas coexist apparently in equilibrium with tourmaline within the tourmaline-rich layers proximal to the aplite-pegmatites. These micas show a pale to almost colorless pleochroism
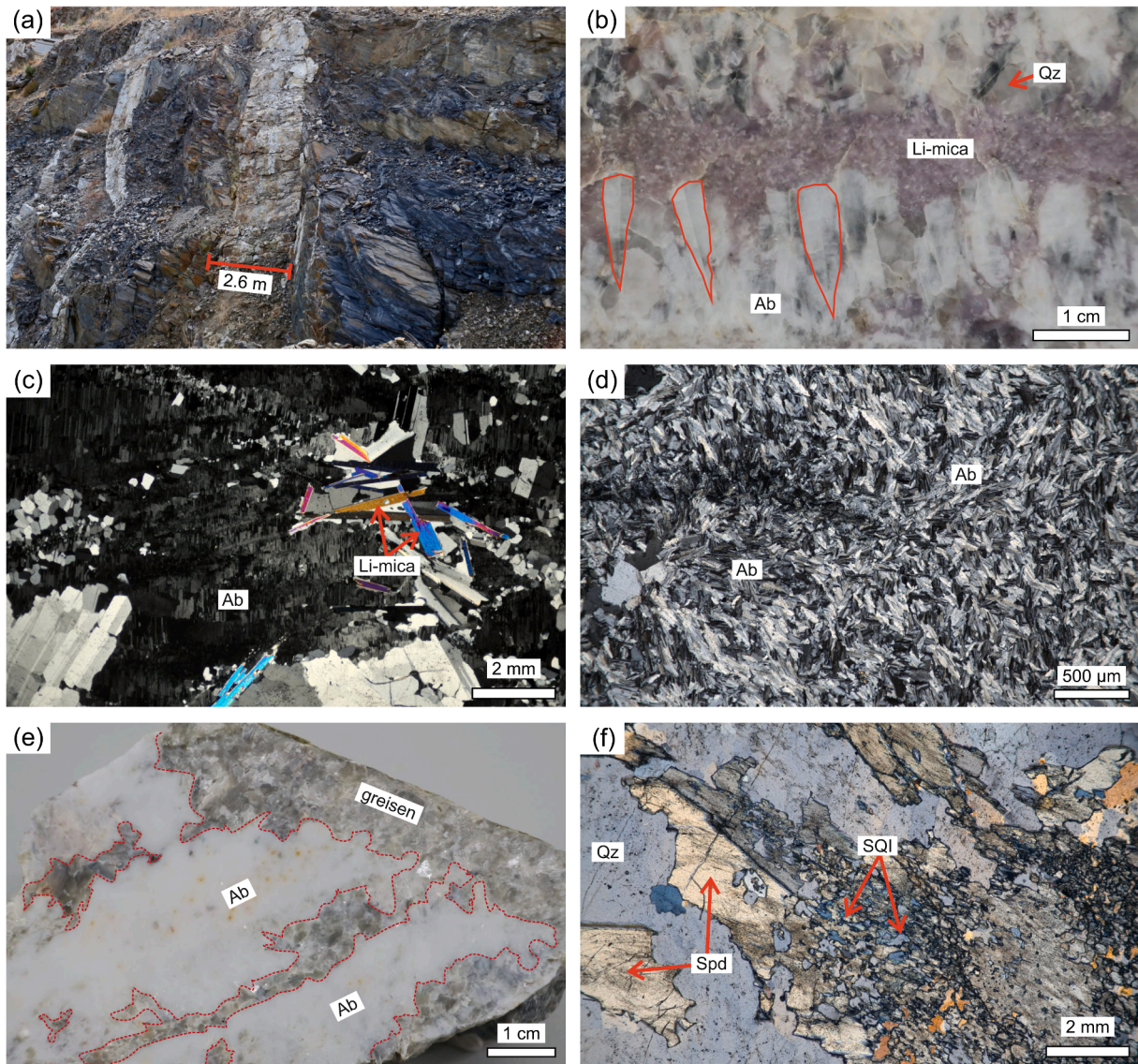
Fig. 2. (a) Photograph of the selected spodumene-bearing aplite-pegmatite dyke from the Alberto open pit. (b) Comb-textured albite (Ab) crystals with their vertex pointing to the wall-rock contact in the Li-mica-bearing dyke from the Feli open pit. (c) 'Chessboard' albite in the Li-mica-bearing aplite-pegmatite. (d) Saccharoidal pure albite, a product of Na-metasomatism. (e) Pegmatite sample showing greisenization via replacement of feldspars by micas + quartz. (f) Secondary spodumene forming spodumene (Spd) – quartz (Qz) intergrowths (SQI).

and are absent in distal samples. Like the tourmaline crystals, their size decreases as the distance from the pegmatite increases. In the first few centimeters from the dykes, where tourmaline prisms comprise almost the entire mineralogy (±quartz), the abundance of these micas is greatly reduced. Beyond these first few centimeters or decimeters, pale-micas become predominant over tourmaline, the latter becoming nearly absent in the psammitic layers (Fig. 5c–f). This association of pale-colored micas and tourmaline in the host rocks occurs in biotite- (and primary muscovite-?) free samples. With increasing distance from the dykes, a zonation of the main mineral assemblage can be simplified as follows: tourmaline ≫ pale-mica + quartz → tourmaline ≈ pale-mica + quartz (±muscovite) → pale-mica ≫ tourmaline + quartz (±muscovite) → biotite + quartz (±muscovite).

Tourmaline-rich layers are significantly more developed near the Hinojosa–Saucelle and Bajoca dykes (thickest dykes), with disseminated tourmaline crystals present 15 m farther from the dyke at Hinojosa–Saucelle. The host rocks of the studied Li-mica-rich aplite-pegmatite from the Feli open pit also display a well-developed tourmalinization, differing from those of the Alberto (spodumene-bearing) dyke. It should

be noted that no petrographic evidence of greisenization or sodic metasomatism were found in the studied metasediments.

5. Whole-rock geochemistry

5.1. Aplite-pegmatite dykes

The four aplite-pegmatite samples from the Fregeneda–Almendra Pegmatite Field have high SiO_2 (70.8–74.3 wt%), Al_2O_3 (15.3–17.7 wt%), Na_2O (2.4–6.3 wt%), and P_2O_5 (0.4–0.9 wt%) contents (Table 3). In contrast, MgO (0.01–0.15 wt%), $Fe_2O_3^t$ (0.4–0.5 wt%), TiO_2 (~0.02 wt%), and CaO (0.2–0.4 wt%) concentrations are relatively low (Table 3). K_2O contents (2.2–7.5 wt%) are variable, and all selected samples are peraluminous to strongly peraluminous, with A/CNK values (Shand, 1943) from 1.11 to 1.99. They are perphosphorous (higher P/Ca than can be accounted for by apatite; cf., Bea et al., 1994), and display K_2O/Na_2O ratios in the range of 0.3–2.2, with the lowest ratios in the aplite-pegmatite from Feli (highest contents of Na_2O and P_2O_5; Table 3).

The studied samples are poor in Ba, Zr, Y, Th, As, W and REE, and are
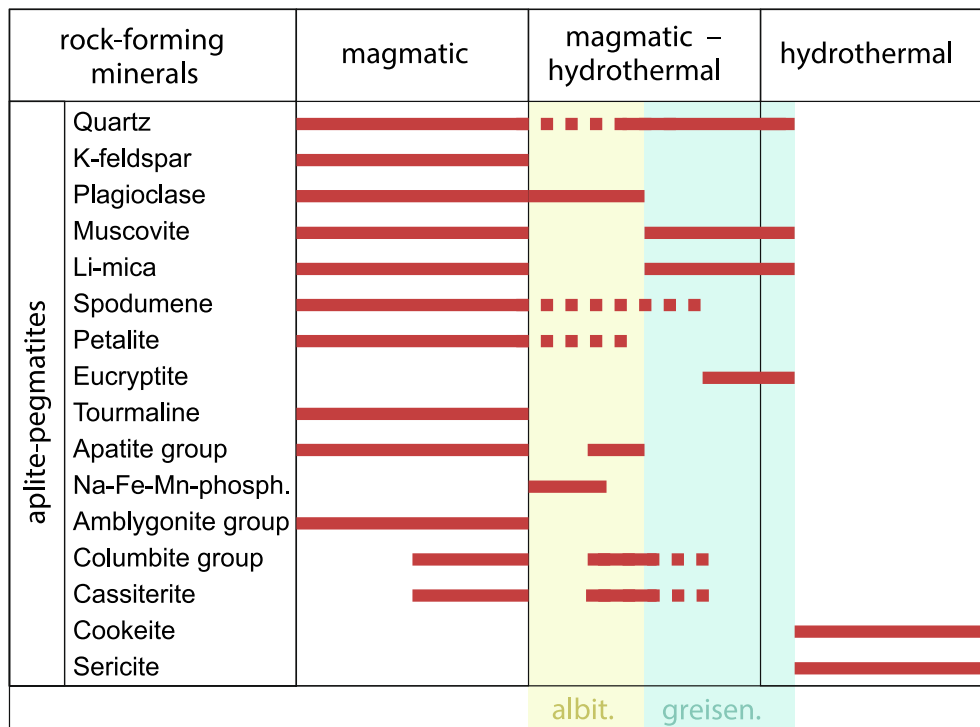
Fig. 3. Paragenetic sequence for studied LCT aplite-pegmatites. Areas of albitization (albit.) and greisenization (greisen.) include mineral phases formed during Na-metasomatism and H⁺-metasomatism, respectively.

enriched in Li, Rb, Cs, Nb, Ta, Sn, Be, Ge, and Tl relative to Iberian granites (Table 3). Fluorine concentrations are relatively low in the pegmatites excepted for the Feli dyke (3100 ppm) (Table 3; Fig. 6a). The highest Be, Ge, Cs, Nb, Ta, Sn and U concentrations were determined for the Feli aplite-pegmatite whereas the highest Li concentration was determined for the Alberto spodumene-bearing pegmatite (9070 ppm). Rubidium concentration is especially high in the intermediate dyke from Tumbo de la Caldera (1310 ppm; Table 3). The Nb/Ta ratio decreases in the selected samples following the sequence, intermediate → petalite- → spodumene- → Li-mica-bearing pegmatite, similar to the K/Rb ratio (Fig. 6b).

5.2. Host metasediments

5.2.1. Major elements

In metasedimentay samples from the Fregeneda–Almendra area, SiO_2 contents are in the range of 53.9–72.5 wt%, and Al_2O_3 contents are 13–21 wt% (Supplementary Table 1). Apart from SiO_2 and Al_2O_3 concentrations, TiO_2, MgO and $Fe_2O_3^t$ contents display small dispersion, with average contents of 0.8, 2.3 and 6.3 wt%, respectively (Supplementary Table 1). Average concentrations of Na_2O and K_2O (1.87 and 4.03, respectively) are similar to that of the Neoproterozoic Iberian Average Shale (NIBAS; Ugidos et al., 2010), and the same is true regarding P_2O_5 (average = 0.15 wt%, discarding anomalous P-rich samples with P_2O_5 >0.45 wt%) (Supplementary Table 1). Excluding Ca-rich control samples Ctrl_01 and Ctrl_02, metasedimentary samples display slightly higher CaO contents in the range 0.14–3.03 wt% compared with that of the NIBAS.

Most of the studied samples plot within the field of shales in the classification diagram of Herron (1988), although some samples project into the greywacke field (Fig. 6c), with SiO_2/Al_2O_3 values in the range of 2.6–5.6. Values of A/CNK fall within the range delimited by the slightly peraluminous Upper Continental Crust (UCC) of Rudnick and Gao (2014) and the NIBAS, showing moderate to strongly peraluminous compositions (A/CNK = 1.17–3.07; Fig. 6d; Supplementary Table 1). The reference composition (RC) given in Table 4 represents an ideal non-

metasomatized composition for the Fregeneda–Almendra metasediments, calculated considering only the collected control samples. In terms of major elements, the concentration of CaO in the RC was calculated excluding the two previously mentioned Ca-rich samples (considering their low representation at regional scale), and the reference P_2O_5 value was obtained discarding samples with P_2O_5 >0.45 wt%.

5.2.2. Trace elements

In comparison with the NIBAS, the metasedimentary samples are rich in Ni, Cr and Th, poor in V, Y, U and Hf, and have similar Zr and Co contents (Supplementary Table 1). Considering only control samples (Table 4), Ba and Rb contents are slightly higher than in the NIBAS and the UCC, whereas Sr concentrations are markedly higher. In multi-element diagrams normalized to the UCC (Fig. 6e), average compositions of regional metasediments display relatively flat patterns close to the UCC composition. Exceptions are marked by positive anomalies of Li, Cs, Rb, F, B, Sn, Be and Tl, as well as by positive Ta and P anomalies and negative Sr anomalies in the case of metasediments from Bajoca (Fig. 6e). Total REE contents vary in the range of 172–286 ppm, and chondrite-normalized REE patterns exhibit segmented geometries, with La_N/Yb_N ratios (~11.2) higher than the NIBAS (Fig. 6f). Heavy REE show nearly flat patterns (Gd_N/Yb_N = ~1.76), contrary to light REE that show moderate slopes (La_N/Sm_N = ~4.14). All samples have similar negative Eu anomalies (Eu/Eu* = $Eu_N/[(Sm_N \times Gd_N)^{1/2}]$) of approximately 0.66 (Fig. 6f). No tetrad effect was observed in the metasomatized metasedimentary samples.

In agreement with the observed anomalies in the UCC multielement diagram, metasomatized samples have significantly high concentrations of F, B, Li, Rb, Cs and Sn (see Table 5 for a compilation of representative metasomatized samples and Supplementary Table 1 for complete results). When the concentrations of these elements are plotted against relative sample distance from the pegmatite, an exponential decreasing trend is observed, which is notable in the most evolved aplite-pegmatites (Figs. 7-9). At these locations (Feli, Alberto, and Hinojosa–Saucelle), Li concentrations in samples close to the pegmatites is about 1500–2000 ppm (Fig. 7a, Fig. 8a and Fig. 9a), with the exception of some chloritized
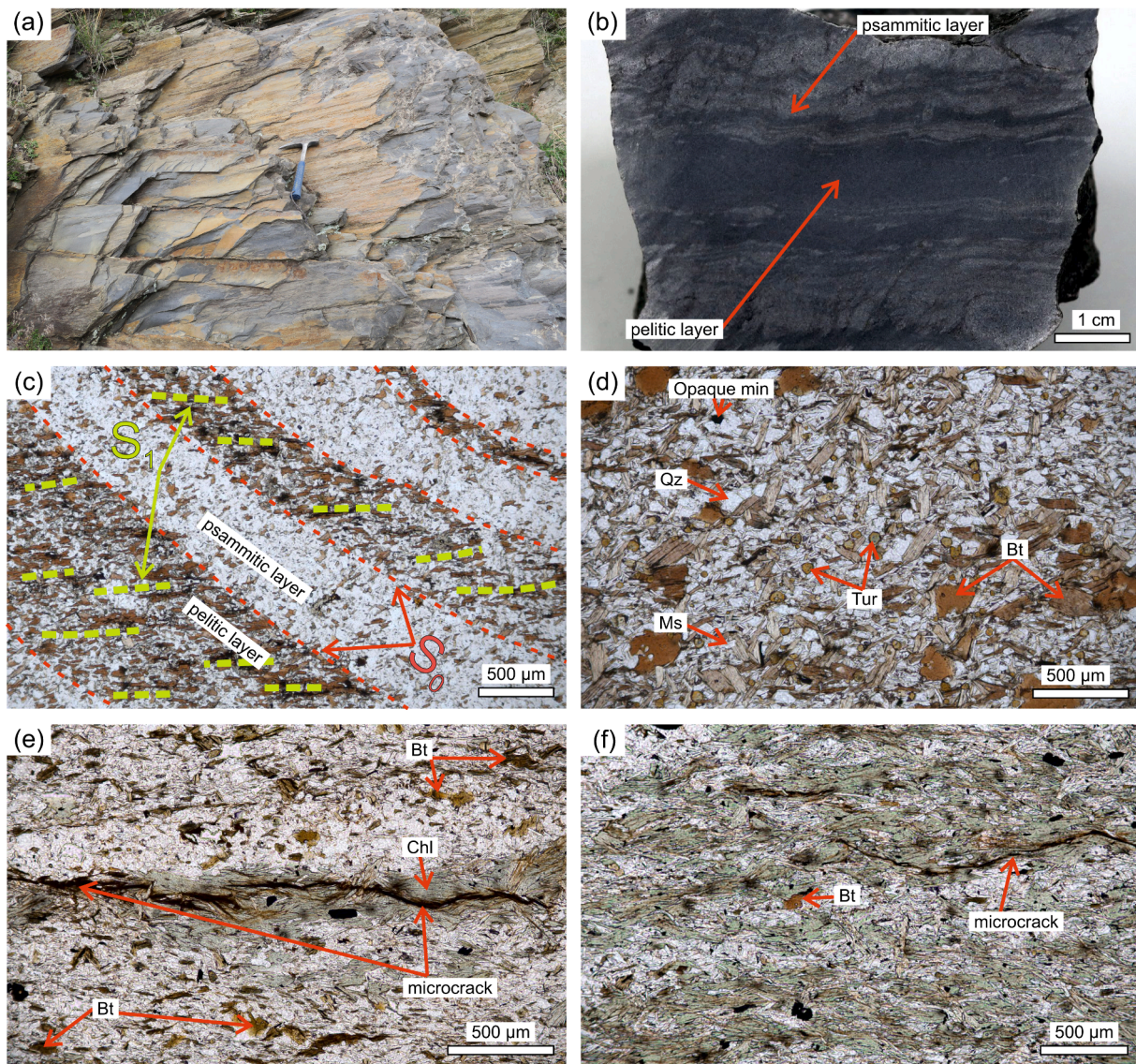
Fig. 4. (a) Field photograph showing representative outcrop of the host psammitic and pelitic metasediments. (b) Section of a metasedimentary hand sample that displays pelitic (dark grey) and psammitic (light grey) laminae. (c) Plane-polarized photomicrograph of alternating psammitic and pelitic layers in host metasediments (S_0 sedimentary layering; S_1 slaty-cleavage). (d) Plane-polarized photomicrograph of biotite (Bt) porphyroblasts developed in pelitic layers constituted by smaller Bt crystals plus quartz (Qz), muscovite (Ms) and tourmaline (Tur). (e) Plane-polarized photomicrograph that shows the development of chlorite (Chl) along microcracks. (f) Strongly chloritized metasedimentary sample with rare fresh biotite flakes.

samples that show relatively low Li contents (e.g., Fig. 9a). Host rocks of the Li-mica-bearing pegmatite show significantly higher values of Cs (1280 ppm) compared with that of the spodumene- and petalite-bearing pegmatites, displaying the highest concentrations between the primary selected dyke and another minor dyke (the other elements mimic this behaviour; Fig. 7). Fluorine concentrations reach extremely high values of 1600–7000 ppm (maximum in the metasediments hosting the Li-mica dyke). Overall, metasedimentary samples closest to the pegmatites have F concentrations higher than the related aplite-pegmatite (Figs. 7-9). Distribution of B is similar to that of F near the most evolved dykes (maximum B is >10000 ppm), excepting the spodumene-bearing pegmatite at Alberto where B concentrations in the host rocks are markedly lower. Rubidium and Sn contents are, in general, higher in the aplite-pegmatites relative to the host rocks, with concentrations up to 1340 ppm Rb and 126 ppm Sn in the most metasomatized samples. Anomalous concentrations of Be (up to 41.0 ppm), Ta (up to 20.2 ppm), Tl (up to 10.4 ppm) and Ge (up to 5.5 ppm), together with As, W, Mo and S were also found in some of the studied samples.

It should be noted that some of the control samples surpass the estimated threshold values of Li and/or Cs for the RC (considering also extensive data compiled in Cardoso-Fernandes et al., 2022), so they were consequently discarded for the calculation of the RC. These anomalous Li and Cs values can possibly be explained by the presence of hidden pegmatite bodies close to those sample sites.

6. Discussion

6.1. Fluid exsolution and pegmatite crystallization

The transition from a magmatic to a pure hydrothermal stage during pegmatite crystallization is a complex multistage process (e.g., Kaeter et al., 2018, 2021; Ballouard et al., 2020; Barros et al., 2020; Hulsbosch and Muchez, 2020; Shaw et al., 2022). The origin and evolution of the pegmatitic melt, particularly emplacement/crystallization pressure conditions and chemical composition of the melt, constrain the nature of the coexisting aqueous liquid (London, 1986; Audétat et al., 2008).
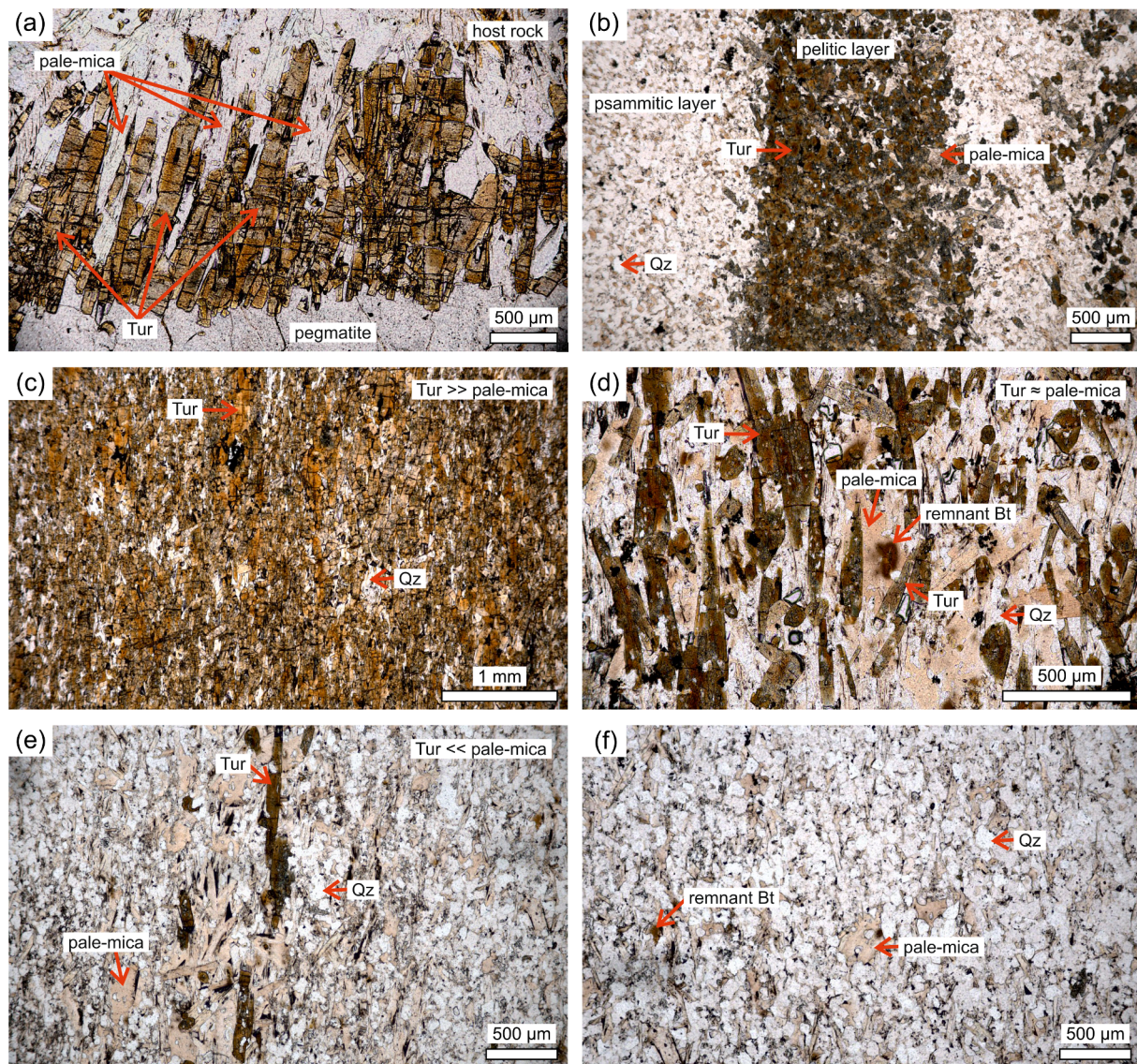
Fig. 5. Plane-polarized photomicrographs of metasomatized metasedimentary samples. (a) Contact between an aplite-pegmatite and its host rocks, with parallelly arranged tourmaline (Tur) crystals developed, in this case, perpendicular to the contact. (b) Tourmaline-rich area strongly controlled by the extent of the pelitic layer. (c) Tourmalinite sample, composed of tourmaline (up to 90% in vol.) and quartz (Qz). (d) Similar tourmaline and pale-mica proportions in a pelitic layer, with remnant biotite. (e) Pelitic layer showing pale-mica predominance over tourmaline. (f) A mainly psammitic layer with pale-micas replacing biotite flakes.

Melt–melt–fluid (silicate melt – hydrosaline melt – aqueous fluid) immiscibility occurs as cooling of the pegmatitic melt proceeds, with aqueous fluids becoming increasingly predominant over hydrosaline melts (Thomas et al., 2012; Kaeter et al., 2018; Ballouard et al., 2020; Hulsbosch and Muchez, 2020). Because aqueous fluids may exsolve at early stages of crystallization or when the complete solidification of the pegmatite is approached, the timing and relevance of aqueous fluid exsolution is still a matter of debate, (e.g., Kaeter et al., 2018). Recent paragenetic studies have linked pegmatite crystallization stages with the continuous transition from magmatic to hydrothermal conditions, identifying overall albitization (Na-metasomatism) and greisenization (H$^+$-metasomatism) as important late-stage processes (Kaeter et al., 2018; Ballouard et al., 2020; Hulsbosch and Muchez, 2020; Shaw et al., 2022).

The subvertical discordant LCT aplite-pegmatite dykes selected for the present study lack a concentric internal zoning and show abundant UST, including layers parallel to the contacts with the host rocks, as well as comb-textured crystals (both ubiquitous across the dykes). Layering in the studied samples may be defined by crystal size or mineralogy,

with alternating pegmatitic and aplitic textures, or alternating albite-rich and Li-mica-rich bands, whereas the most common comb crystals are those of alkali feldspars, spodumene and petalite. Unidirectional solidification textures have been attributed to rapid crystallization far from equilibrium, induced by strong undercooling conditions (Webber et al. 1997, 1999; Sirbescu et al., 2008; Nabelek et al. 2010). The undercooling may be prompted by a sudden change of pressure or temperature, or by a chemical fluctuation, such as a decrease of important fluxing components (e.g., B, P, F and Li) in the melt (e.g., Simmons and Webber, 2008; London, 2018). In addition, the observed variation in crystal size could result from significant sudden changes in the nucleation density as a function of the liquidus undercooling, with pegmatitic layers formed at low-nucleation density and aplitic bands at high density (Simmons and Webber, 2008; Nabelek et al. 2010; London, 2018). The occurrence of several thin alternating pegmatitic and aplitic layers in a single dyke would indicate that the undercooling vs nucleation density and undercooling vs growth rate curves (see Nabelek et al. 2010) should be very close, which would allow slight changes in the physical-chemical conditions during crystallization to favour either the

Table 3

Major- (wt%) and trace-element (ppm) whole-rock geochemical analyses of selected aplite-pegmatites from the Fregeneda–Almendra Pegmatite Field.

Locality	Feli	Alberto	Hinojosa-Saucelle	Tumbo de la Caldera
Type	Li-mica	Spodumene	Petalite	Intermediate
Thickness (m)	1.8	2.6	7.0	1.2
Sample	FEL-02	ALB-01	PET-01	BAR-06
SiO_2	70.84	74.27	74.29	71.04
TiO_2	0.02	0.02	0.02	0.02
Al_2O_3	17.07	16.79	15.30	15.91
$Fe_2O_3^t$	0.45	0.36	0.38	0.50
MnO	0.03	0.02	0.03	0.04
MgO	0.04	0.15	0.01	0.05
CaO	0.32	0.21	0.43	0.30
Na_2O	6.30	2.44	5.41	3.44
K_2O	2.15	3.74	3.78	7.46
P_2O_5	0.82	0.37	0.48	0.67
LOI	1.00	0.86	0.71	0.63
Total	99.07	99.26	100.90	100.10
F	3100	< 100	100	200
As	7	< 5	7	< 5
B	50	20	50	< 10
Ba	27	20	52	29
Be	208	94	89	71
Bi	< 2	< 2	< 2	< 2
Cd	< 2	< 2	< 2	< 2
Co	1.3	0.6	0.6	0.9
Cr	70	70	100	70
Cs	379	57.2	28.5	40.7
Cu	27	10	8	12
Ga	38.2	15.1	15.7	19.6
Ge	13.6	4.0	4.1	4.1
Hf	4.8	< 0.2	0.6	0.4
In	< 0.2	< 0.2	< 0.2	< 0.2
Li	2600	9070	200	61
Mo	< 1	1	2	2
Nb	78.1	22.1	12.6	10.3
Ni	30	30	40	20
Pb	20.2	12.7	35	13.4
Rb	1080	772	640	1310
S	< 0.01	< 0.01	< 0.01	< 0.01
Sb	< 2	< 2	< 2	< 2
Sc	< 0.1	0.1	0.1	0.2
Se	< 8	< 8	< 8	< 8
Sn	768	93.2	61.1	34.6
Sr	75	50	82	45
Ta	118	14	6.7	3.5
Te	< 6	< 6	< 6	< 6
Th	3.1	0.4	0.2	0.2
Tl	7.7	6.2	4.3	10.4
U	8.9	1.5	1.7	1.2
V	< 5	< 5	< 5	< 5
W	3.9	< 0.7	0.9	3.0
Y	0.2	0.6	0.6	1.4
Zn	< 30	50	40	40
Zr	38	3	11	7
La	< 0.4	0.6	< 0.4	0.7
Ce	< 0.8	< 0.8	< 0.8	0.9
Pr	< 0.1	0.1	< 0.1	< 0.1
Nd	< 0.4	0.5	0.6	0.7
Sm	< 0.1	0.2	< 0.1	0.2
Eu	< 0.1	< 0.1	< 0.1	< 0.1
Gd	< 0.1	< 0.1	< 0.1	0.2
Tb	< 0.1	< 0.1	< 0.1	< 0.1
Dy	< 0.3	< 0.3	< 0.3	< 0.3
Ho	< 0.2	< 0.2	< 0.2	< 0.2
Er	< 0.1	< 0.1	< 0.1	< 0.1
Tm	< 0.1	< 0.1	< 0.1	< 0.1
Yb	< 0.1	< 0.1	< 0.1	0.2
Lu	0.02	0.08	< 0.01	0.01

aplitic or the pegmatitic texture. At this point, it should be highlighted that OH^--and H_2O-bearing minerals, such as micas, are scarce in the studied subvertical dykes. If these pegmatites crystallized from portions of melts expelled from the apical part of a magma chamber, where a previous vertical chemical zoning occurred with accumulation of fluxing components in the upper parts (see Roda-Robles et al., 2016, 2018; Garate-Olave et al., 2017, 2020), then they should be relatively rich in H_2O and probably not far from H_2O-saturation. Consequently, the paucity of hydrated minerals within the dykes could be caused by the early exsolution of a fluid phase favoured by the sudden adiabatic decompression (first boiling), produced by the intrusion of pegmatitic melts in open fractures at brittle upper crustal conditions. Early exsolution of an aqueous fluid phase, with significant amount of fluxing components (e.g., B, F and Li), would certainly induce a chemical quenching of the pegmatitic melts (e.g., Garate-Olave et al., 2020). In addition, a concomitant sudden temperature drop originated by the intrusion of pegmatitic melts into significantly colder host rocks would enhance the undercooling of the melt. The combination of the chemical, thermal and baric undercooling would result in a rapid crystallization of the pegmatitic melts under disequilibrium conditions, leading to a complete crystallization in a short period of days–weeks according to modelling developed by Webber et al. (1997, 1999) for similar dyke-like pegmatites. Moreover, the studied dykes are usually thin (<5 m), which may have reduced thermal insulation of their core, thus preventing a slower crystallization rate. Collectively, these factors would result in the formation of internally unzoned dykes with abundant UST textures like those found at Fregeneda–Almendra.

The strong tourmalinization observed in the host rocks, proximal to the dykes, suggests open-system behaviour during pegmatite intrusion and early exsolution of a fluid phase. This aqueous liquid would sequester most of the B, as suggested by the absence of tourmaline and low B concentrations in the evolved aplite-pegmatites. In addition to B, other important fluxes, such as Li, F and P, would be transported contemporaneously by the aqueous solution to the host rocks. While B-metasomatism is spatially restricted close to the pegmatite contacts, Li-metasomatism (together with Cs, Rb, Sn and F) becomes rapidly predominant with increasing distance from the dykes (Figs. 7-9). After the early release of fluids that metasomatize the host rocks, the subsequent crystallization of dominantly anhydrous minerals under isobaric conditions in the aplite-pegmatites may prompt H_2O saturation (second boiling). Thus, during cooling/crystallization of the pegmatitic melt, a second metasomatic event could occur, with no evidence of it in the host rocks and, therefore, assumed to have developed exclusively within the aplite-pegmatites (auto-metasomatism). Based on the paragenetic sequence observed in the studied dykes (simplified in Fig. 3), the Na-metasomatism as indicated by albitization of feldspars, presence of saccharoidal pure albite and other evidence described in section 4.1, preceded lower-T greisenization. The generation of H^+ during albitization (hydrolysis of earlier silicates) leads to a decrease of the pH (increasing acidity) in the saline hydrothermal fluid, which induces greisenization (e.g., Kaeter et al., 2018; Ballouard et al., 2020). Because greisen masses are spatially reduced in (and probably restricted to) the studied aplite-pegmatites, a low fluid/rock ratio may be assumed for the second metasomatic event. The large proportion of fluids expelled in the first metasomatic event may cause a drastic reduction of the fluid/rock ratio during the second event. Moreover, if the second boiling occurred when the crystallization was advanced, or nearly complete, the crystallized portion of the intrusion may have inhibited fluid release. The considerably lower permeability of the pegmatite at this advanced/completed crystallization stage would even preclude the release of such fluids into the host rocks, as it seems to be the case of the studied aplite-pegmatites. A final, purely hydrothermal alteration stage was also expressed in the studied dykes, resulting in the formation of cookeite and sericite (Fig. 3). Leaving aside the second (auto-)metasomatic event, a detailed study of the early metasomatism is presented in the following section.
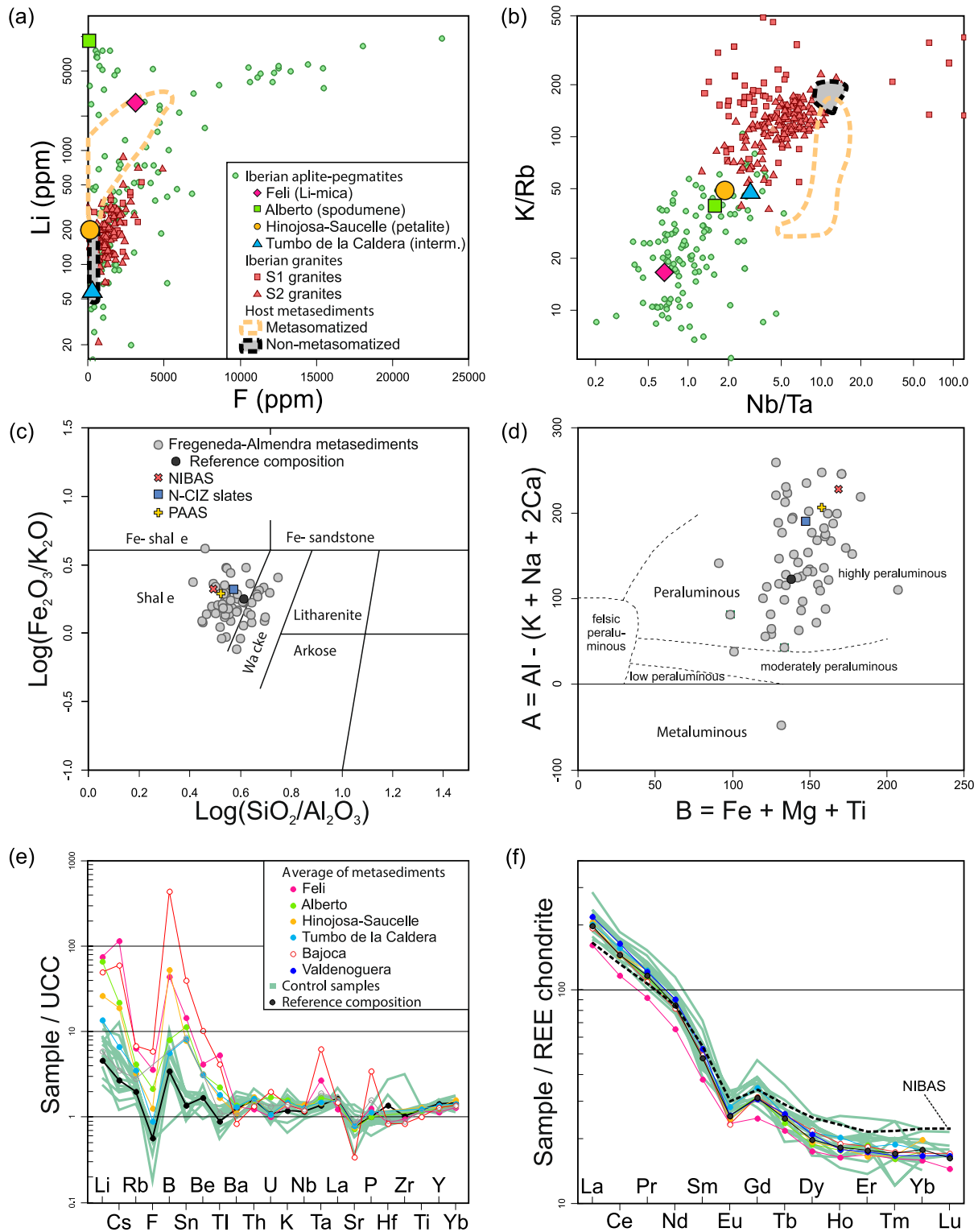
Fig. 6. (a) Bivariate plot displaying F vs Li (logarithmic) concentrations of selected aplite-pegmatites (Iberian aplite-pegmatites, S_1 granites and S_2 granites taken from Roda-Robles et al., 2018). (b) Nb/Ta vs K/Rb diagram (logarithmic) for the studied aplite-pegmatites (legend as in Fig. 6a). (c) Classification diagram for siliciclastic sediments (Herron 1988), showing compositions of the studied metasedimentary host rocks (and the reference composition for Fregeneda–Almendra). Compositions of the Neoproterozoic Iberian Average Shale (NIBAS; Ugidos et al., 2010), average of North-Central Iberian Zone (*N*-CIZ) slates (Villaseca et al., 2014) and the Post Archean Australian Shale (PAAS; Taylor and McLennan, 1985) are also displayed for comparison. (d) Multicationic [B] vs [A] diagram of Debon and Le Fort (1983) modified by Villaseca et al. (1998) (legend as in Fig. 6c). (e) Spider plots for the metasediments normalized to Upper Continental Crust (UCC; Rudnick and Gao, 2014). (f) Chondrite-normalized (McDonough and Sun, 1995) REE diagrams for the studied metasediments (legend as in Fig. 6e).

Table 4

Major- (wt%) and trace-element (ppm) whole-rock geochemical analyses of metasedimentary control samples and the reference composition for the regional metasediments.

	Control Samples														Ref.[*]
	Ctrl 01	Ctrl 02	Ctrl 03	Ctrl 04	Ctrl 05	Ctrl 06	Ctrl 07	Ctrl 08	Ctrl 09	Ctrl 10	Ctrl 11	Ctrl 12	Ctrl 13	Ctrl 14	
	Control samples considered after the geochemical study							Control samples discarded after the geochemical study[**]							
SiO_2	63.5	67.12	61.24	65.29	63.18	65.38	69.74	62.45	60.93	64.85	62.44	63.47	63.03	64.98	65.06
TiO_2	0.72	0.7	0.81	0.73	0.81	0.824	0.842	0.84	0.88	0.76	0.83	0.8	0.78	0.82	0.78
Al_2O_3	15.18	15.43	18.04	16.06	17.12	16.99	14	18.01	19.4	16.24	17.97	17.51	17.86	16.56	16.12
$Fe_2O_3^t$	5.55	5.53	7.7	6.29	6.19	6.09	4.18	6.53	6.4	6.41	6.35	6.25	5.8	6.06	5.93
MnO	0.151	0.088	0.098	0.067	0.077	0.062	0.047	0.058	0.06	0.073	0.074	0.061	0.051	0.066	0.08
MgO	2.13	2.24	2.69	2.3	2.22	2.14	1.44	2.69	2.82	2.47	2.64	2.2	2.17	2.58	2.17
CaO	7.95	3.81	1.4	2.1	2.62	0.83	1.01	1.16	0.43	1.57	1.16	1.73	1.12	1.4	1.59
Na_2O	0.71	2.24	1.84	1.96	2.9	1.88	2.76	2.16	1.02	2.48	1.83	2.62	1.32	2.05	2.04
K_2O	1.84	2.41	4.01	3.72	4.02	4.28	3.2	4.69	5.87	3.89	5.15	4.11	5.04	3.91	3.35
P_2O_5	0.15	0.16	0.14	0.12	0.14	0.13	0.2	0.09	0.14	0.13	0.12	0.16	0.13	0.13	0.15
LOI	1.81	0.89	2.08	1.88	1.01	2.19	2.18	1.93	2.49	1.5	1.92	1.42	2.31	1.78	–
Total	99.74	100.7	100.1	100.6	100.3	100.8	99.61	100.6	100.4	100.4	100.5	100.3	99.61	100.3	–
F	300	400	400	300	100	400	300	300	300	400	300	200	300	300	314
As	< 5	17	< 5	< 5	< 5	< 5	8	5	5	5	7	5	6	8	< 5
B	< 10	70	70	60	50	48	56	60	90	50	60	60	110	180	59.0
Ba	642	611	827	633	1100	933	706	897	1250	836	997	792	994	1020	779
Be	4	3	4	5	4	3	2	3	4	3	3	4	3	3	3.57
Bi	< 2	< 2	< 2	< 2	< 2	1	< 0.4	2	2	2	2	2	2	2	< 2
Cd	< 2	< 2	< 2	< 2	< 2	NA	NA	2	2	2	2	2	2	2	< 2
Co	15.3	15.7	17.3	15.6	14.7	24	12	12.3	15.3	15.7	14.7	15.8	17	11.5	16.4
Cr	120	110	130	130	140	90	110	140	140	130	130	120	120	120	119
Cs	6	23	25.5	9.7	11.4	9.5	7.6	13.8	45	18.2	24.9	10.3	27.8	62.6	13.2
Cu	17	17	35	29	8	20	10	14	5	20	14	17	20	11	19.4
Ga	20.7	23.2	30.8	24.6	24	24	17	29.4	31.1	22.9	27	27.7	29.1	24.7	23.5
Ge	2.3	2.6	2.5	1.9	2.2	2	1	3.2	2.1	2.2	2.5	2.3	1.8	2.3	2.07
Hf	5.4	5.3	4.6	NA	9.8	4.3	14.6	NA	NA	NA	NA	NA	NA	NA	7.33
In	< 0.2	< 0.2	< 0.2	< 0.2	< 0.2	< 0.2	< 0.2	0.2	0.2	0.2	0.2	0.2	0.2	0.2	< 0.2
Li	83	150	94	113	129	60	50	186	226	291	178	186	181	158	97.0
Mo	2	< 1	< 1	< 1	< 1	< 2	3	1	1	1	1	1	1	1	< 1
Nb	11.4	12.9	15.5	13.2	15.1	18	12	15	15.7	12.9	14.7	16.9	15.1	15.7	14.0
Ni	40	40	60	50	50	30	30	50	50	70	60	40	40	30	42.9
Pb	28.3	22.4	24.2	23.3	34.7	21	21	20.3	12	21.7	18.7	24.6	16.4	16.6	25.0
Rb	121	138	207	197	185	182	141	208	240	196	238	190	232	177	167
S	0.02	< 0.01	0.02	< 0.01	< 0.01	NA	NA	0.01	0.01	0.01	0.01	0.01	0.01	0.01	< 0.01
Sb	< 2	< 2	< 2	< 2	< 2	< 2	< 2	2	2	2	2	2	2	2	< 2
Sc	12.1	11.6	15.7	NA	13.6	15	11	NA	NA	NA	NA	NA	NA	NA	13.2
Se	11	< 8	20	11	11	NA	NA	8	8	42	11	11	16	31	13.3
Sn	2.7	1.9	3.7	1.9	2.8	4	3	2.9	4.2	3.1	4.2	2.2	4	3.7	2.86
Sr	448	381	190	294	343	191	228	264	117	239	243	276	187	296	249
Ta	1	1.1	1.4	1.2	1.4	1.3	1.2	1.3	1.4	1.4	1.6	1.5	1.1	1.1	1.23
Te	14	9	14	15	15	NA	NA	18	23	13	13	19	15	17	13.4
Th	14.3	14.5	16.5	15.8	16.9	14.7	22.7	17	18.6	15.9	16.7	18.3	17	16.7	16.5
Tl	0.5	0.7	0.9	0.6	1	0.9	1.1	1.1	1	1.2	1.2	0.8	1	0.9	0.81
U	2.9	2.5	3.2	2.3	2.9	2.7	4.1	2.4	2.7	3.2	2.6	3.5	2.2	3.7	2.94
V	75	75	101	82	86	97	74	99	109	85	103	87	92	97	84.3
W	1.5	1.2	2.2	1.6	2.4	3	2	2.9	2.5	1.6	2.4	1.7	2.7	2.5	1.99
Y	26.9	33.7	30.2	25.5	29.4	33	32	25.4	30.3	25.3	27.4	33.3	23.2	26.7	30.1
Zn	80	100	110	90	80	90	60	90	90	90	80	90	80	60	87.1
Zr	207	233	175	NA	214	171	612	NA	NA	NA	NA	NA	NA	NA	200
La	42.2	67.7	56.2	40.7	53.1	46.1	51	45.6	54.5	47.1	51.7	55.9	44.7	49.5	51.0
Ce	84.3	114	103	91.3	102	90.2	106	89	106	84	91.2	107	93.4	96.5	98.7
Pr	9.4	14.2	12	9.9	12.6	10.2	11.9	10.4	12.4	10.9	11.7	13.4	10.7	11.6	11.5
Nd	35.4	52.5	45	36.7	44.8	37.3	44	38.4	43.3	40.4	43	45.3	37.8	39.4	42.2
Sm	6.6	10.6	8.3	6.6	8.4	6.8	8.2	6.2	7.6	5.8	8.2	9.6	7.1	7.9	7.93
Eu	1.4	1.7	1.9	1.5	1.8	1.56	1.68	1.9	1.8	1.6	1.7	1.5	1.6	1.8	1.65
Gd	6.3	9.3	7.3	6.1	7.8	6	6.7	5.6	7.7	6.3	7.6	7.2	7.1	7.8	7.07
Tb	1	1.3	0.8	0.9	1	0.9	1	0.8	0.9	0.8	1	1.1	0.7	1	0.990
Dy	4.1	6.4	5.1	4.4	5.9	5.7	5.7	4.6	5.2	4.7	5.5	5.9	4.9	5.2	5.33
Ho	0.9	1.3	0.9	0.8	1	1.1	1.1	0.9	1.1	0.9	1.1	1.4	1	1	1.01
Er	2.5	3.3	3.2	2.2	2.9	3.3	3.4	2.8	3.2	2.9	3.1	4	3	3.1	2.97
Tm	0.5	0.6	0.5	0.4	0.4	0.48	0.49	0.4	0.3	0.3	0.4	0.6	0.4	0.5	0.480
Yb	2.9	2.6	3.2	2.5	2.6	3.1	3.5	2.7	2.6	2.6	2.3	3.6	2.7	2.8	2.91
Lu	0.44	0.41	0.41	NA	0.42	0.46	0.53	NA	NA	NA	NA	NA	NA	NA	0.450

NA not analyzed.

"-" not calculated.

[*] Reference composition calculated from control samples (n = 7), excluding anomalous samples (for CaO and P_2O_5), and metasomatized samples.

[**] Discarded due to their relatively high Li contents of >150 ppm (see text for explanation).

Table 5

Major- (wt%) and trace-element (ppm) whole-rock geochemical analyses of highly enriched (metasomatized) metasedimentary samples from the Fregeneda–Almendra Pegmatite Field.

Locality	Feli	Feli	Feli	Alberto	Alberto	Alberto	Hinojosa-Saucelle	Hinojosa-Saucelle	Hinojosa-Saucelle	Bajoca	Bajoca
Dyke type	Li-mica	Li-mica	Li-mica	Spd.	Spd.	Spd.	Ptl.	Ptl.	Ptl.	Ptl.	Ptl.
Distance* (m)	0	1	1.8	0	0.5	0	0	0.5	12	0.5	0
Sample	FR-49	FR-51	FR-52	F-38	F-39	F-43	FR-18	FR-19	FR-24	BJ04-B-DD	BJ04-D-DD
SiO_2	67.59	58.46	66.23	66.85	63.52	65.32	53.90	61.76	58.89	68.05	64.64
TiO_2	0.67	0.95	0.71	0.76	0.77	0.91	0.80	0.89	0.89	0.55	0.58
Al_2O_3	14.40	20.79	15.07	15.70	17.44	15.87	20.98	17.79	20.47	14.68	16.77
$Fe_2O_3^t$	5.41	6.14	5.34	5.30	6.51	5.58	8.97	6.96	7.34	5.96	5.74
MnO	0.11	0.05	0.09	0.07	0.05	0.08	0.11	0.13	0.08	0.09	0.09
MgO	1.95	2.43	1.77	1.98	2.55	2.21	3.36	2.67	2.71	2.02	2.02
CaO	2.01	0.56	1.40	1.85	0.66	1.77	2.56	1.35	1.70	0.80	1.64
Na_2O	2.25	2.37	1.58	3.00	1.17	1.88	4.00	1.80	1.78	0.41	0.54
K_2O	2.62	5.09	4.42	3.74	5.28	3.33	3.77	3.50	1.75	3.22	2.97
P_2O_5	0.16	0.14	0.61	0.15	0.12	0.20	0.13	0.17	0.58	0.61	1.22
LOI	1.62	2.76	2.13	1.04	2.06	2.23	1.68	2.54	2.59	2.23	2.60
Total	98.82	99.76	99.41	100.50	100.20	99.27	100.50	99.52	98.82	98.60	98.83
F	3400	3100	7000	2400	700	1800	1600	1300	2700	3100	3400
As	45	73	148	31	7	26	41	18	281	466	1080
B	420	3900	910	250	220	110	470	2240	> 10,000	6090	8880
Ba	972	1310	590	1000	894	681	620	850	566	294	280
Be	10.0	14.0	22	11.0	4.0	12.0	13.0	9.0	17.0	41.0	29
Bi	<2	<2	<2	<2	<2	<2	<2	<2	<2	<0.4	0.4
Cd	<2	<2	<2	<2	<2	<2	<2	<2	<2	NA	NA
Co	7.8	9.4	8.3	11	15.2	11.3	11	15.5	8.8	11	15
Cr	100	160	110	120	140	130	140	140	140	90	100
Cs	1120	668	1280	169	107	130	270	157	76.4	306	230
Cu	7	17	11	6	31	30	16	18	22	10	10
Ga	21.3	35.2	24	23.4	27	27.5	29.3	25.2	29	18	20
Ge	2.5	3.9	4.5	2.6	2.3	2.9	3.5	2.8	5.5	2	3
Hf	5	4.2	6.7	NA	NA	NA	NA	NA	NA	3	3.8
In	<0.2	0.3	<0.2	<0.2	<0.2	<0.2	<0.2	<0.2	<0.2	<0.2	<0.2
Li	1990	2530	4120	1920	1530	1750	1450	1070	281	1270	1120
Mo	<1	2	2	<1	1	<1	<1	<1	4	2	2
Nb	13.2	16.8	24.1	16.3	15.8	14.6	14.9	17.1	22.1	11	16
Ni	40	40	40	40	60	40	60	50	50	30	40
Pb	16.9	16.4	13.1	32	13.5	38.1	64	23.2	39.7	7	13
Rb	762	786	1340	417	342	507	523	378	163	665	557
S	<0.01	0.12	<0.01	<0.01	<0.01	0.02	<0.01	<0.01	0.02	NA	NA
Sb	<2	<2	<2	<2	<2	<2	<2	<2	<2	<2	<2
Sc	10	18.2	10.5	NA	NA	NA	NA	NA	NA	10	11
Se	<8	10	<8	<8	<8	<8	<8	<8	<8	NA	NA
Sn	38.5	64.8	117	48	18.9	48.4	35.6	39.1	81.4	105	126
Sr	397	152	301	355	148	214	480	249	235	81	185
Ta	1.5	1.5	11.9	2.7	1.4	1.3	1.3	1.3	2	3.5	20.2
Te	15	18	13	20	20	16	<6	<6	<6	NA	NA
Th	9.9	20.8	11.9	15.5	16.9	15.3	19.8	16.6	17.4	9.7	11
Tl	7.6	5.9	10.4	2.7	2	3	3.8	2.4	0.8	4.8	4.5
U	2.3	2.9	3.4	4.1	7.3	5.8	3.4	2.8	2.9	3.7	4.1
V	72	112	69	81	92	86	117	99	109	73	77
W	18.4	8.4	13.7	1.7	3	33.8	2	2.5	11.1	8	11
Y	14.7	28.8	24.7	22.7	27.9	31.5	17.5	28.4	24.5	24	27
Zn	80	80	100	190	80	190	180	730	170	130	200
Zr	206	154	261	NA	NA	NA	NA	NA	NA	127	140
La	20.4	56.5	38.7	48.3	51.8	48.8	54.1	46.1	45.1	32	33.7
Ce	36.8	114	63	92.1	97	91.2	95.3	82.8	84.2	63.5	64.9
Pr	4.5	13.2	8.2	10.8	11.3	10.9	12.2	11.2	10.2	7.2	7.55
Nd	16.9	46	32.2	39.7	39.1	41	41.3	39.5	36.8	26	27.6
Sm	2.8	8	5.1	6.4	8.3	7.6	6.3	7	5.7	5.3	5.8
Eu	1	2	1.5	1.4	1.4	1.5	1.6	1.2	1.3	0.86	1.17
Gd	2.8	6.5	6.1	5.6	6.3	6.4	5	6.2	5.5	5.2	5.4
Tb	0.3	1	0.9	0.9	0.9	1	0.6	0.9	0.9	0.9	0.8
Dy	2.7	4.7	4.5	4.4	5.2	5.3	3	5	4.7	5	4.8
Ho	0.6	1	0.9	0.8	0.9	1.1	0.5	1	1	1	0.9
Er	1.6	3	2.2	2.4	2.9	3.5	1.9	2.7	2.5	2.8	2.7
Tm	0.2	0.5	0.3	0.3	0.4	0.5	0.3	0.4	0.4	0.4	0.39
Yb	1.6	3.1	2.6	1.9	2.6	3.2	2	3.4	3.9	2.6	2.5
Lu	0.23	0.49	0.33	NA	NA	NA	NA	NA	NA	0.37	0.39

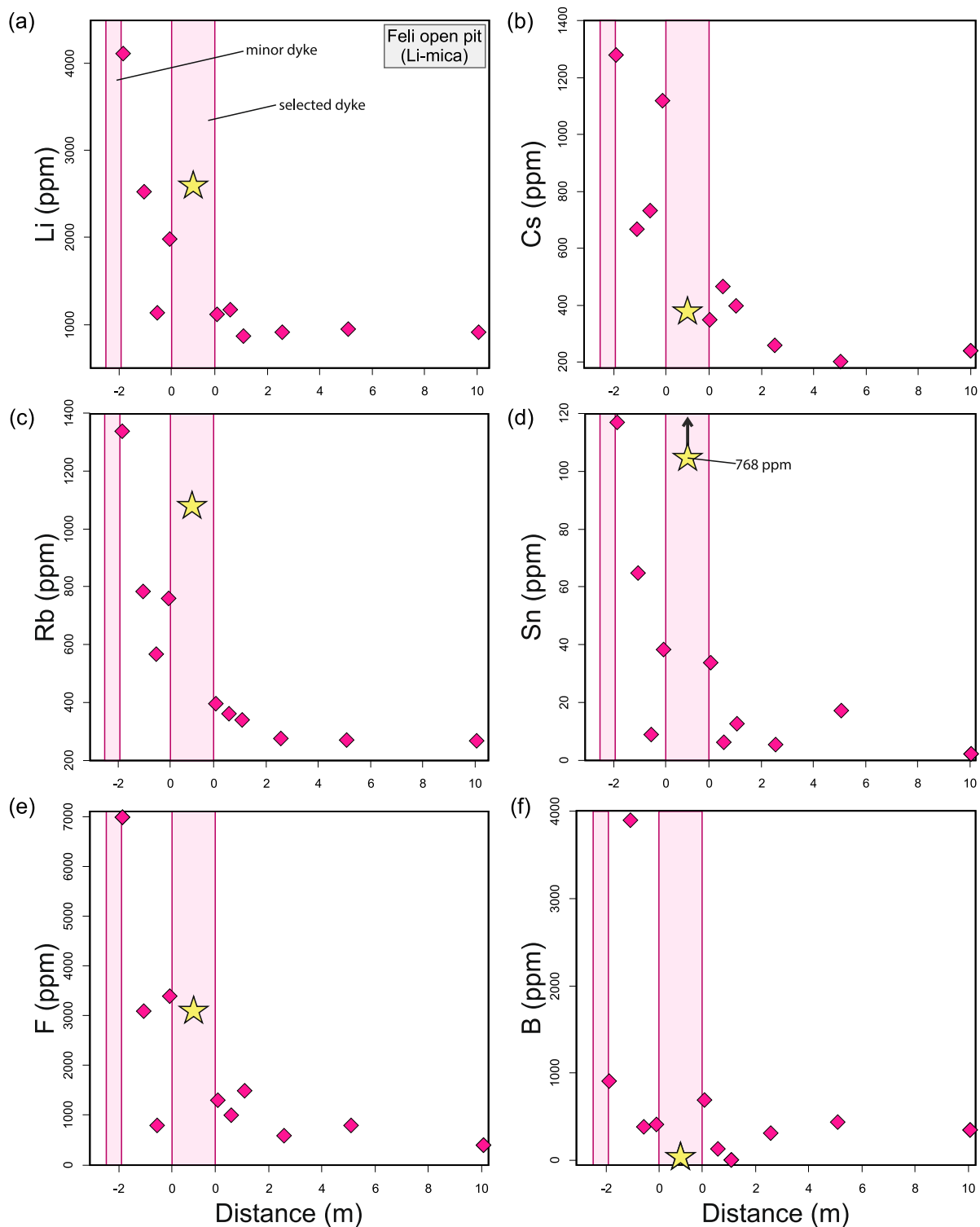NA not analyzed.

* Distance from the dyke.

Fig. 7. Plots of distance vs trace element concentration for metasomatized metasedimentary samples from the Feli open pit. The stars mark the concentration of respective elements in the Li-mica-bearing pegmatite.

6.2. Metasomatism of metasediments by intrusion of aplite-pegmatites

Metasomatic alteration of host rocks caused by the intrusion of LCT pegmatites involves mainly enrichment in alkali elements (e.g., Li, Rb and Cs) and volatiles (e.g., H_2O, F and B) (Shearer et al., 1984; Morgan and London, 1987; Černý, 1989; Selway et al., 2005). At Fregeneda–Almendra, the early exsolution and release of an aqueous phase from the pegmatitic melt into the host rocks has resulted in an enrichment of

these elements (e.g., Figs. 7-9). The structural relationship between the subvertical dykes and metasedimentary host rocks is effectively the same at the four main sample sites; therefore, this variable can be omitted. However, the heterogeneously distributed and variably developed chloritization, postdating pegmatite emplacement and present at all localities, should be taken with caution as it could modify features of prior metasomatism (e.g., Fig. 9). With this consideration, it was noted that the Chemical Index of Alteration (CIA; Nesbitt and Young, 1982) of
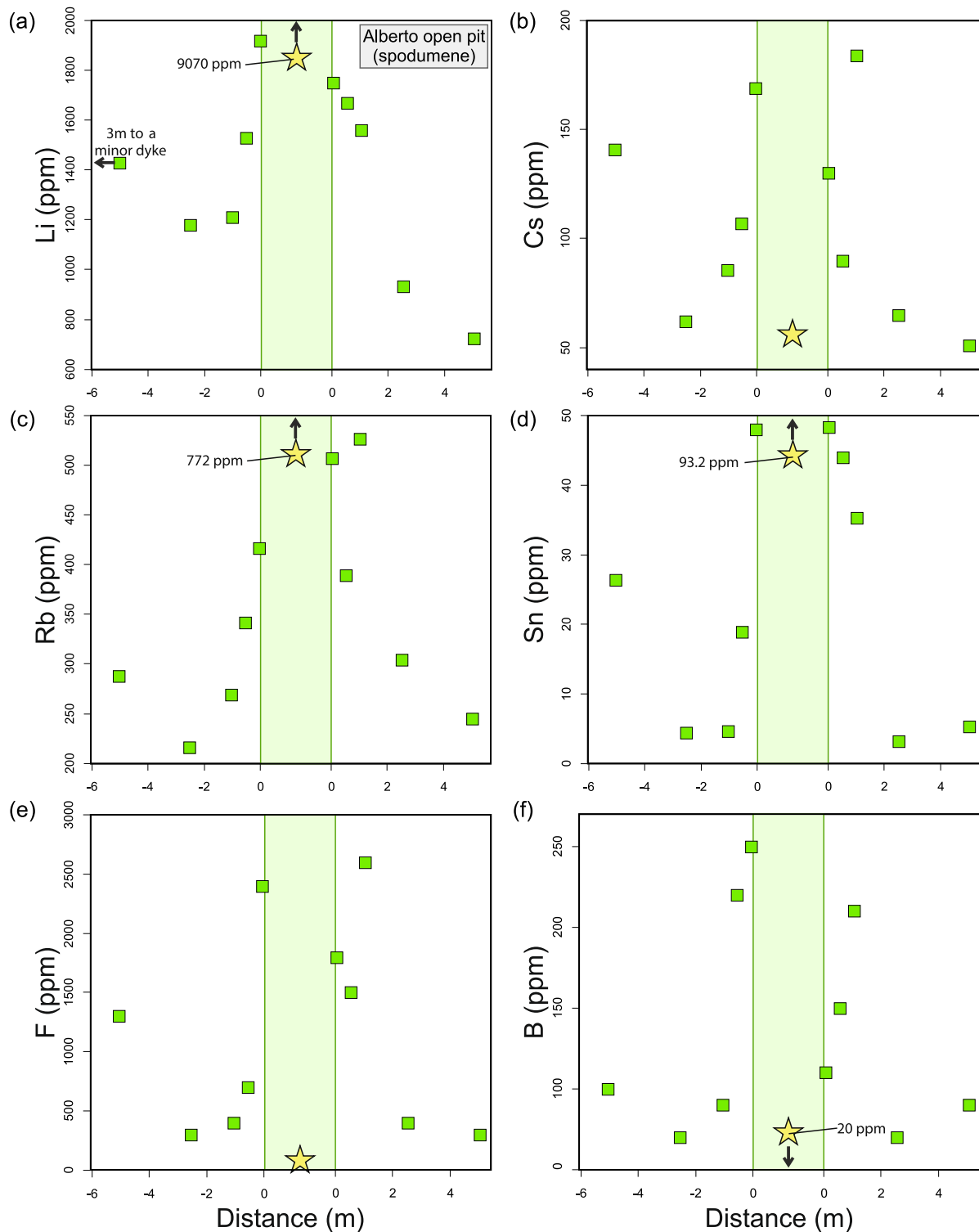
Fig. 8. Plots of distance vs trace element concentration for metasomatized metasedimentary samples from the Alberto open pit. The stars mark the concentration of respective elements in the spodumene-bearing pegmatite.

strongly chloritized samples in this study is typically > 68. CIA values were calculated as CIA = $[Al_2O_3 / (Al_2O_3 + CaO^* + Na_2O + K_2O)] \times$ 100, where oxides are in molar proportions and CaO* represents the CaO of the silicate fraction (Fedo et al., 1995). The previous observation is in agreement with other works on similar metasediments from the Iberian Massif, where low CIA values are considered to indicate minimal weathering or a limited degree of post-depositional alteration (i.e., fresh rocks) (see Fuenlabrada et al., 2016, 2021; Rojo-Pérez et al., 2021),

whereas CIA values of >70 would represent minor to moderate weathering (Fuenlabrada et al., 2020). Overall, CIA values in metasediments from Fregeneda–Almendra are lower than 70 (55–70), and only strongly chloritized samples (also showing high loss on ignition [LOI] values of >3 wt%) display greater values than about 70, together with some Ca-rich and apatite-rich samples (Fig. 10).
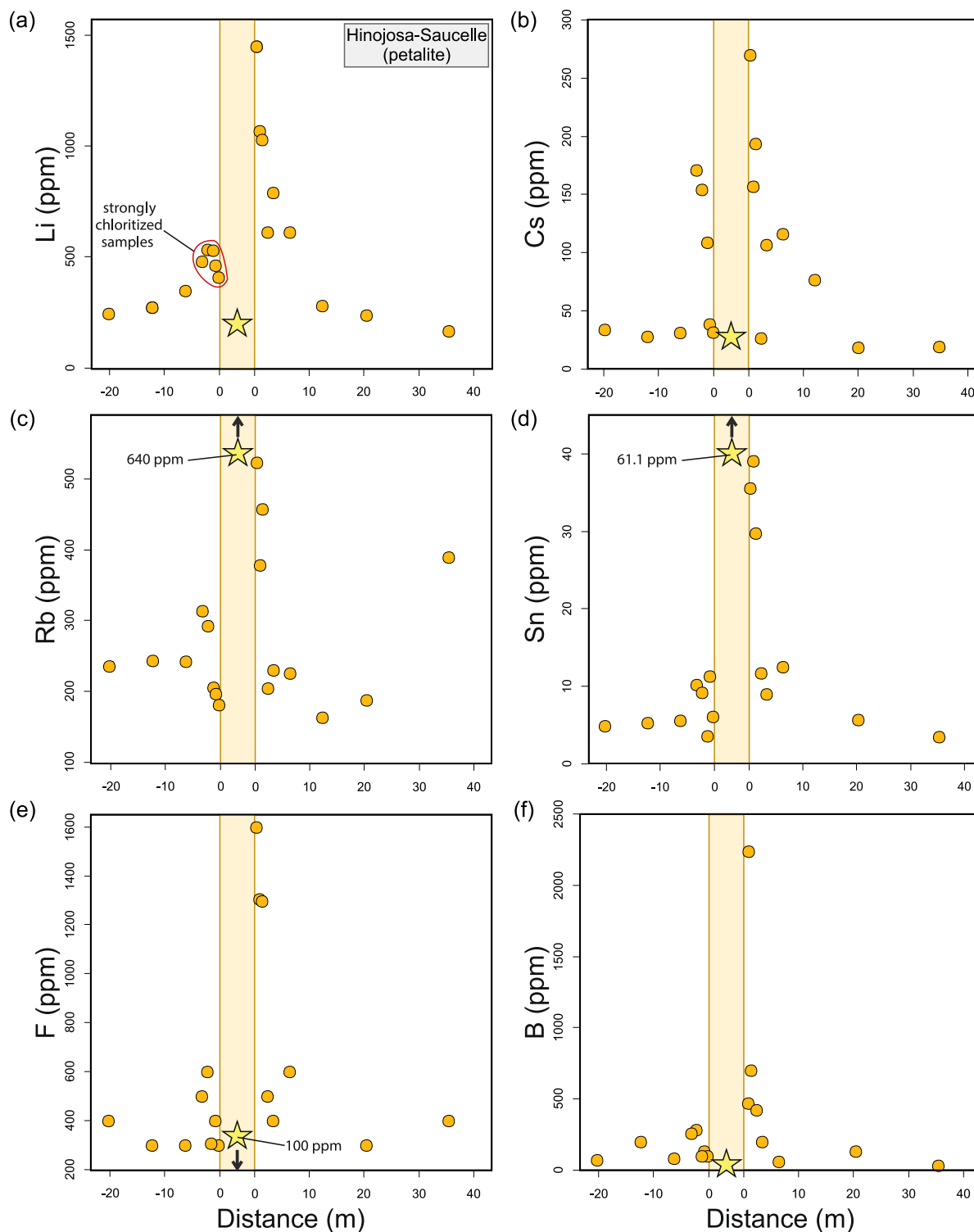
Fig. 9. Plots of distance vs trace element concentration for metasomatized metasedimentary samples from Hinojosa–Saucelle. The stars mark the concentration of respective elements in the petalite-bearing pegmatite.

6.2.1. Selection of immobile elements

Quantification of whole-rock chemical gains and losses was performed following the Isocon method proposed by Grant (1986) after Gresens' (1967) equation for composition–volume relations during metasomatic alteration. The assumption that at least one component behaves as immobile in a determined metasomatic system leads to the categorization of elements as relatively mobile or immobile (Gresen, 1967). In this work a set of immobile elements, those with no difference in concentration between metasomatized and non-metasomatized samples, was used as a reference frame (Fig. 11). The calculated reference composition shown in Table 4 was used as the non-metasomatized composition for these calculations. An ideal immobile element would display a slope C_i^a / C_i^0 of 1 on the 'Isocon diagram' (if volume remains constant or significant mass-change did not occur, as in the studied case); therefore, elements with a slope of 1.0 ± 0.1 were considered as immobile in this study (Supplementary Table 2).

Freseneda-Almendra metasediments

- ■ Samples with CaO/Na₂O > 1
- ▲ Apatite-rich samples (P₂O₅ > 0.41 wt. % in whole-rock)
- ● Control samples
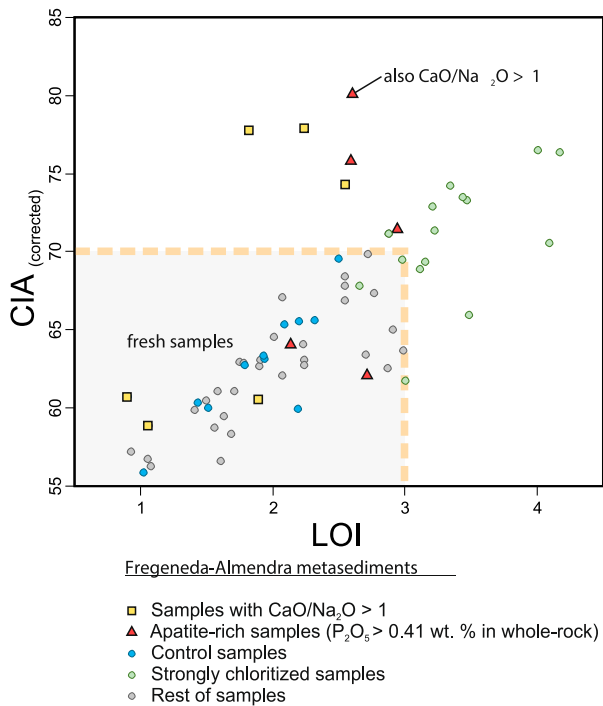- ● Strongly chloritized samples
- ● Rest of samples

Fig. 10. Loss on ignition (LOI) vs Chemical Index of Alteration (CIA) diagram, where strongly chloritized samples display overall CIA values of > 68–70 and LOI values of > 3 wt%. Correction of the CIA was carried out following McLennan (1993), with a first calculation of CaO in apatite considering whole-rock P₂O₅ data (CaO$_{ap}$ = CaO – 10/3 × P₂O₅), and a later comparison of CaO$_{ap}$ with whole-rock Na₂O (if CaO$_{ap}$ > Na₂O, then CaO* = Na₂O; if CaO$_{ap}$ < Na₂O, then CaO* = CaO$_{ap}$).
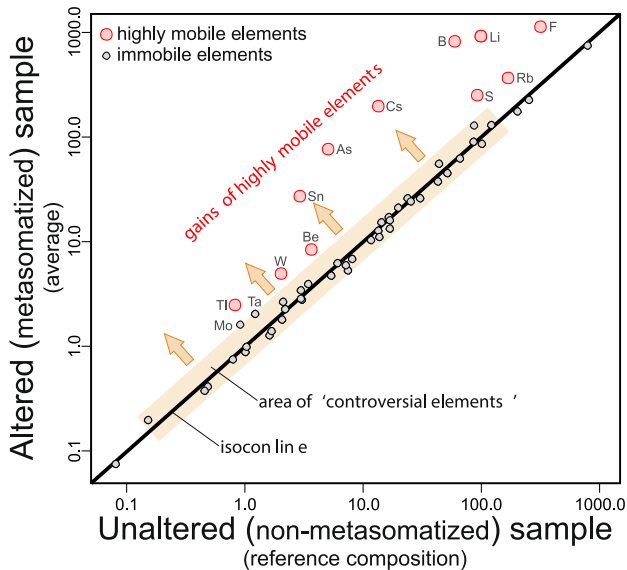

Fig. 11. Isocon diagram (after Grant, 1986, 2005) for the studied metasediments, considering the reference composition from Table 4 as the unaltered (non-metasomatized) sample and total average contents of all metasomatized samples (Supplementary Table 1) as the altered (metasomatized) sample. See text for the explanation of 'controversial elements.'. Isocon line: $C_i^a / C_i^0 = 1$; $\Delta C_i = C_i^a - C_i^0 = 0$, where C_i^a is the concentration of an element "i" (in wt% or ppm) in a metasomatized sample, and C_i^0 is the concentration of the element "i" in a non-metasomatized sample.

Averages of major elements, excepting P₂O₅, CaO and K₂O, have consistent C_i^a / C_i^0 slopes of 1.0 (±0.1). The slope of 1.4 calculated for P₂O₅ is the result of some apatite-rich rocks sampled close to some of the dykes, while variations of CaO and K₂O are not controlled by the distance from the dyke, but rather by inherited chemical variations from the sedimentary protolith. Similarly to most major elements, a number of high-field strength elements (Zr, Nb, Y, Ga, Sc, Th, Pb), large ion lithophile elements such as Sr and Ba, some transition metals (Cu, Cr, V) and REE behave as immobile, showing average C_i^a / C_i^0 slopes of 1.0 ± 0.1 (Supplementary Table 2). To calculate gains and losses, the set of immobile elements was reduced in order to make the results from different localities comparable. The best regression to fit the Isocon line in each sample leads to the selection of Si, Al and Ti as the consistently immobile elements reliable for mass-balance calculations, with comparable slopes of the respective Isocon lines (1.00 ± 0.13; Supplementary Table 2). This selection was tested by means of cluster of slopes (least-squares regression method using EASYGRESGRANT of López-Moro, 2012), composition-volume diagrams (Gresen, 1967; Potdevin, 1993), and the 'Isocon diagram' (Grant, 1986, 2005). The authors would like to point out that no quartz veining was observed in the metasomatized samples, nor any other evidence of later quartz dissolution-precipitation, which supports the assignment of Si as an immobile element.

6.2.2. Determination of highly mobile elements

The selection of immobile elements allows identification of those elements that behave as highly mobile. It must also be considered that some elemental variations reflect the original composition, obscuring the recognition of those elements enriched by external (metasomatic) effects. These 'controversial elements' usually display greater variation in C_i^a / C_i^0 slopes than immobile elements, but not at magnitudes comparable to highly mobile elements (e.g., Fig. 11). For the Fregeneda-–Almendra Pegmatite Field, the minimum slope to discern highly mobile elements and those elements of questionable mobility is marked by Rb. Due to the relatively high background concentrations of Rb in the studied metasediments (see the reference composition of Table 4), the enrichment of Rb is defined by a slight average slope of 2.2 (Supplementary Table 2). Consequently, elements that display average slopes >2.0 were considered as highly mobile in the studied samples, and the enrichment of these elements attributed to external processes. The calculated average C_i^a / C_i^0 slopes leads to the classification of F, B, Li, Rb, Cs, Sn, Be, Tl, As, W and S (±Mo, Ta) as highly mobile elements (Fig. 11; Supplementary Table 2). In general, higher concentrations of F, B, Cs, As, W and S are found in the metasomatized host rocks when compared with the aplite-pegmatites, in contrast to Li, Rb, Sn, Be and Tl (e.g., Figs. 7-9). This suggests that these elements are strongly partitioned into the early exsolved fluid phase in preference to the pegmatitic melt consistent with published fluid-melt partition coefficients (e.g., London, 1986; Pollard et al., 1987; Simon et al., 2007; Hulsbosch et al., 2016; Binder et al., 2018; Audétat, 2019). Moreover, other elements also display C_i^a / C_i^0 ratios too high to be considered as immobile. Among these 'controversial elements', P, Ge, Ta, and Te are commonly enriched in LCT pegmatites (e.g., London, 1987; Černý and Ercit, 2005; Selway et al., 2005; Márquez-Zavalía et al., 2012; Garate-Olave et al., 2017), and Mo (together with S) is partitioned into the vapor phase in similar evolved granitic systems (Tingle and Fenn, 1984). All of these mobile elements would be dissolved in the early exsolved aqueous fluid that was expelled from the aplite-pegmatites into the host rocks, some of them showing a clear preference for the fluid phase over the pegmatitic melt.

6.2.3. Quantification of gains and losses during mass-transfer

Whole-rock elemental gains and losses during metasomatism can be approached through absolute quantifications, where the concentration of an element "i" in the non-metasomatized (C^0) sample is added or subtracted from the metasomatized (C^a) samples ($C_i^a - C_i^0$). Following this procedure, elements with maximum absolute gains are B (9941

ppm), F (6700 ppm) and Li (4023 ppm), with lower absolute gains for Cs (1266 ppm), Rb (1173 ppm), S (1150 ppm), As (1077 ppm), and Sn (167 ppm), and minor gains in the case of Be, W, and Tl (Fig. 12a; see Supplementary Table 2 for detailed results). However, the foremost parameter used to calculate mass-transfer in metasomatic systems is the relative gain and loss of an element "i", expressed as $\Delta C_i^a / C_i^0 = (1/M \times C_i^a / C_i^0) - 1$ (Grant, 1986, 2005), where M represents the slope of the Isocon. The obtained numerical results (Supplementary Table 2) indicate that, among the highly mobile elements, highest relative maximum gains are observed for As (357) and B (155), followed by Cs (101), Sn (57), and Li (43), and lowest gains are found for F, S, W, Tl, Be and Rb (<22) (Fig. 12b).

To analyze the effect of the aplite-pegmatite types, the distances from the dyke (for each of the collected samples) have been normalized to the thickness of the related dyke (relative distance in Fig. 13 and Supplementary Table 2). At all localities, gains of highly mobile elements are highest in close proximity to the pegmatite margin, and decrease away from the dyke margin. Arsenic, W and S are exceptions because their enrichment is not strictly related to distance from the pegmatite. In the case of Li, the observed trends for relative grain/loss approach the reference composition (no relative gain) at distances of about 4–5 times the thickness of the dyke for Feli (Li-mica-bearing pegmatite) and Alberto (spodumene-bearing pegmatite) (Fig. 13a). At Hinojosa–Saucelle (petalite-bearing pegmatite) and Tumbo de la Caldera (intermediate pegmatite), relative Li gains approach the RC at distances twice the width of the dyke (Fig. 13a). It is noteworthy that those samples that occur relatively close to a second dyke (in between two dykes) show superposed enrichments, falling outside of the overall trend defined by other samples. Strongly chloritized samples that display low relative gains also fall outside of the overall trend (Fig. 13c). The behavior of Cs is similar to that of Li, with the highest relative gains in the Li-mica-bearing dyke (background values reached at distances >6 times the thickness of the dyke). Cesium gains reach background values at a relative distance of ~3 for the petalite- and spodumene-bearing dykes, with the lowest gains in samples from the barren and intermediate dykes (Fig. 13b). The extent of the metasomatic halo for Rb is slightly narrower than those of Li and Cs, with the greatest gains surrounding the Li-mica-bearing dyke of the Feli open pit (Fig. 13c). Gains of Sn differ from other elements because the maximum enrichments are observed at Bajoca (petalite-bearing dyke) (Supplementary Table 2). In addition, there are no clear differences in Sn, F and B gains between the selected sites, which may be best represented by a general decreasing trend from relatively high gains to that of the RC within distances equal

to the width of the dykes (Fig. 13d–f).

The first inference from the quantification of gains resulting from the early metasomatism caused by the aplite-pegmatites is that the metasomatic haloes become greater (in distance and gains) as the fractionation degree of the pegmatitic melts increases. Considering the evolutionary trend of discordant aplite-pegmatites from Fregeneda–Almendra (types 6 to 9) gains of highly mobile elements are considerably lower in host rocks of the intermediate dykes, as expected, and the highest gains are associated with the most evolved dykes containing Li-mica (Fig. 13). Among the highly mobile elements, enrichment in B, F, Li, Cs, Rb, Sn, Be and Tl in the host rocks is inversely correlated with distance from the dyke (Fig. 13). It seems evident that the highest mass-transfer during metasomatism of studied LCT pegmatites is that of B > F > Li > Cs > Rb (Fig. 12a), but that these absolute gains are not strictly correlated with the relative gains (B > Cs > Sn > Li > F; Fig. 12b). Enrichments of other mobile elements such as P, Ge, Ta, Te and Mo, represented by local or minor gains in the host rocks, are also likely related to the release of the early exsolved fluid from the aplite-pegmatites. In this system, lithium is the most mobile element (in agreement with observations made by Selway et al., 2005), followed closely by Cs (Fig. 13). The relative mobility of Rb is more difficult to interpret; depending on the original Rb contents in the host rocks the resulting C_i^a / C_i^0 slope could be too low to consider it highly mobile.

6.3. Implication of metasomatic aureoles in mineral exploration

The metasomatic haloes surrounding aplite-pegmatites from the Fregeneda–Almendra area resemble those from other case studies of LCT pegmatites (Morgan and London, 1987; Černý, 1989; Selway et al., 2005; Linnen et al., 2012), with elevated gains of B, F, Li, Cs, Rb and Sn (±Be, Tl) (Fig. 12). The outward-decreasing trends at the studied localities indicate that each highly mobile element behaves differently, with distinct degrees of enrichment at a determined distance (Fig. 13). An important outcome from this study for mineral exploration is that an estimation of 'proximity indicator concentrations' could be calculated from the trends of Fig. 13. These concentrations (or higher) would indicate relative proximity to a buried dyke at Fregeneda–Almendra, with Li and Cs as the most useful mobile elements. Thus, Li contents of about 200 ppm (or higher) in the metasedimentary samples from the area (or equally ~30 ppm of Cs), would indicate proximity to a (hidden) mineralized dyke, with Rb (~300 ppm) and Sn (15 ppm) as complementary indicators (Fig. 14). Despite the consistent outward-decreasing trends for some mobile elements, F and B do not show clear trends with
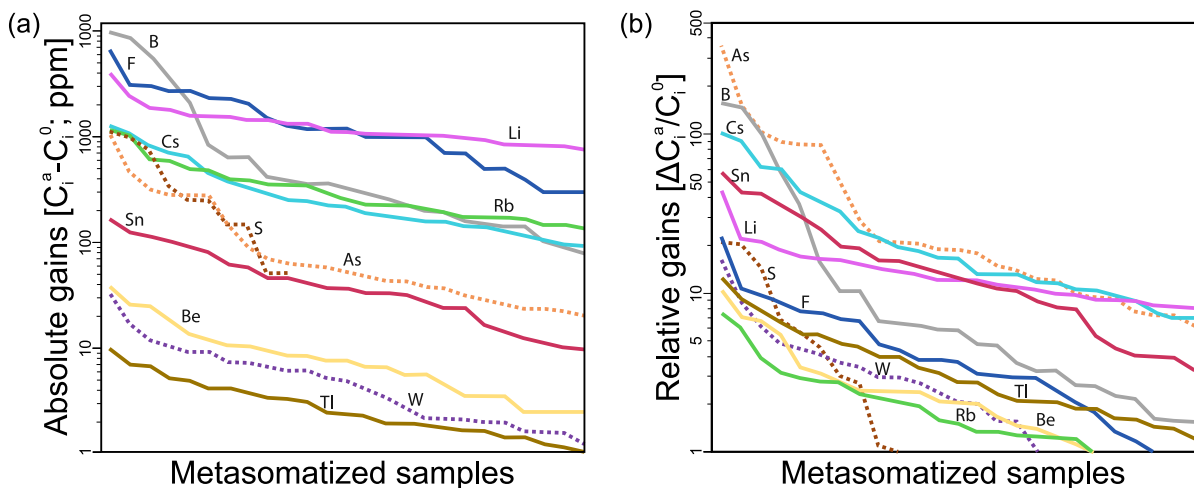
Fig. 12. Diagrams with absolute (a) and relative (b) gains (y-axis logarithmic) of highly metasomatized samples. For each element, the 25 most metasomatized samples were selected. Their gains are arranged according to a decreasing trend to aid visualization (the order of the 25 metasomatized samples in the x-axis differs in each decreasing trend without respect to distance from a pegmatite dyke).
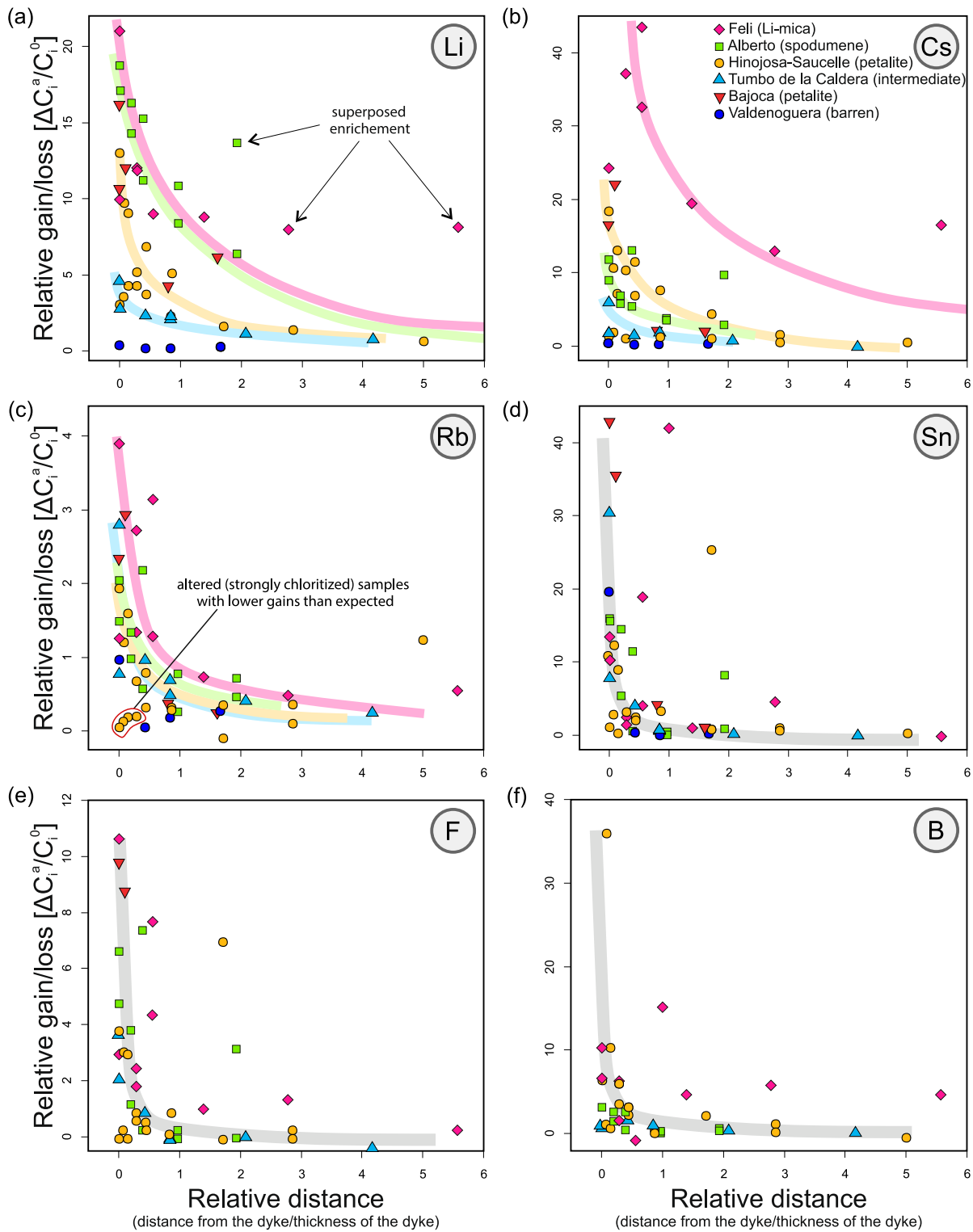
Fig. 13. Diagrams of relative distance (distance from the dyke normalized with the thickness of the dyke) vs relative gain/loss for (a) Li, (b) Cs, (c) Rb, (d) Sn, (e) F, (f) B.

respect to a certain dyke, and these data should be treated with caution in terms of geochemical exploration. Another notable observation is that the CIA and LOI could be useful parameters for geochemical exploration in this pegmatite field. Chemical Index of Alteration values >70 in these types of metasediments, together with high LOI values (>3 wt%), could suggest a pervasive (post-metasomatic) chloritization process that may cause significant leaching of highly mobile elements (Figs. 9, 10 and 13).

Careful documentation of chloritization is important as these samples can obscure the determination of geochemical trends within a particular geochemical halo, leading to an erroneous estimation of the proximity to a buried or unexposed aplite-pegmatite. Moreover, some metasedimentary samples show extremely high enrichments in certain highly mobile elements (e.g., ~4000 ppm of Li, ~1300 ppm of Cs, ~1300 ppm of Rb), which are often higher than concentrations in the related
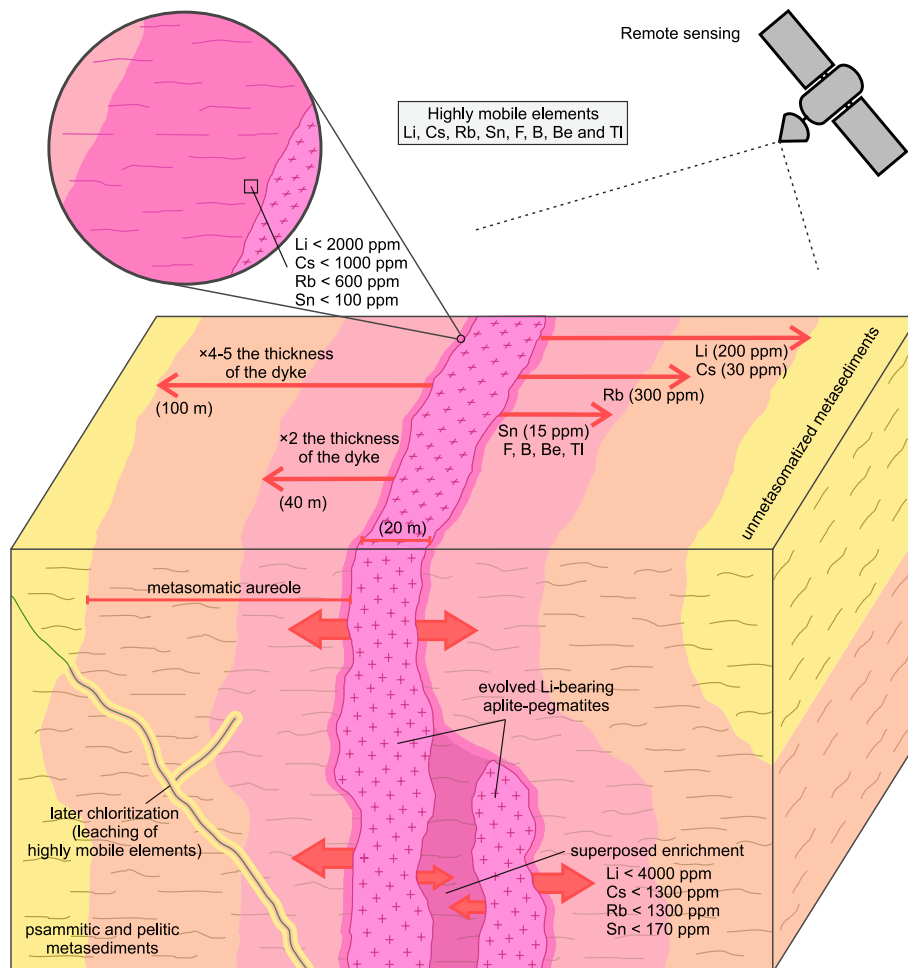
Fig. 14. Idealized schematic representation of a metasomatic aureole generated by the intrusion of an evolved aplite-pegmatite in the Fregeneda–Almendra Pegmatite Field.

pegmatite dyke. Such anomalous concentrations could signify the superposition of metasomatic haloes, and therefore, may indicate the presence of multiple evolved aplite-pegmatite dykes (Fig. 14).

Considering relative distances and calculated gains for the selected haloes, an economically interesting pegmatite dyke of about ~20 m in width would generate a metasomatic halo with enrichment in Li-Cs and Rb-sn-(±F, B) of up to ~100 and 20–40 m, respectively (Fig. 14). Considering that at Fregeneda–Almendra evolved pegmatite dykes are nearly subvertical and that the host metasediments show a similar structural relationship (Roda-Robles et al., 1999, 2010; Vieira et al., 2011), an important outcome of this work is the recognition of extensive surficial representation of the geochemical haloes generated by dykes with economic potential. A geochemical halo, in the case of Li and Cs, would cover a longitudinal area of up to 220 m (20 m dyke + [2×100 m halo]), or in terms of significant gains of >2, one of about 100 m (20 m dyke + [2×40 m halo]) (Fig. 14).

This imprint caused by the pegmatitic intrusions at Fregeneda-–Almendra could be present in other pegmatitic fields with similar host rocks. Taking into account the location of known Li-mineralization in the Iberian Massif (e.g., Roda-Robles et al., 2018), the obtained results could be used to aid exploration for buried mineralized pegmatites in large areas of this Variscan Belt segment. The geochemical signature of the studied Neoproterozoic to lower Paleozoic host metasediments could help to constrain the most prospective areas. Despite some slight geochemical differences compared with those equivalent series in the CIZ (e.g., lower Ti/Nb and Yb/Th ratios or higher CaO concentrations than NIBAS), overall, compositions of the studied host rocks resemble those of the Neoproterozoic to lower Paleozoic successions ascribed to the Schist–Greywacke Complex (e.g., similar SiO_2/Al_2O_3, Zr/Sc, La/Th and Cr/V ratios) (see Ugidos et al., 1997, 2003, 2010; Villaseca et al., 2014).

The size of these metasomatic anomalies (up to 200 m) makes them potentially detectable with the use of remote sensing techniques (e.g., Cardoso-Fernandes et al., 2019, 2020). Moreover, most of the highly mobile elements in the metasomatic haloes can be semi-quantitively analyzed in the field using portable tools such as X-ray Fluorescence (XRF) and Laser-Induced Breakdown Spectroscopy (LIBS; e.g., Fabre et al., 2021; Xing et al., 2021) equipments, thus expediting pegmatite discovery. Prospect scale studies analogous to this one provided for Fregeneda–Almendra, with detailed characterization of the pegmatite-related metasomatic haloes, will further enhance the reliability and performance of these techniques.

7. Conclusions

1) The intrusion of LCT aplite-pegmatite dykes generated metasomatic haloes of variable size in the psammitic and pelitic host metasediments in the Fregeneda–Almendra Pegmatite Field (CIZ). The sudden adiabatic decompression of the system led to a strongly undercooled pegmatitic melt and the early exsolution (and expulsion) of an aqueous fluid. This fluid was responsible for the formation of the exocontact metasomatism, with tourmaline and pale-micas as the main metasomatic minerals.

2) Early exsolution of the metasomatizing fluids depleted the pegmatitic melts in volatiles and some metals, and late-stage fluid exsolution was mainly restricted within the pegmatites. During this late-magmatic to hydrothermal stage, albitization and greisenization processes resulted basically in pegmatite auto-metasomatism.

3) Quantification of whole-rock chemical gains and losses shows that F, B, Li, Rb, Cs, Sn, Be, Tl, As, W and S (±Mo, Ta) behaved as highly mobile elements during metasomatism. Excluding As, W, and S (±Mo), gains of the other fluid-mobile elements decrease exponentially with the distance from the pegmatite contacts.

4) First evidence of anomalous concentrations of highly mobile elements was observed at distances of 4–5 times the thickness of the dykes. Significant relative gains of >2 are observed at distances of 1–2 times the thickness of the dykes or closer.

5) The spatial extent and magnitude of element enrichment of metasomatic aureoles is closely related with the pegmatite type. The geochemical haloes are expanded as the degree of fractionation in the pegmatitic melts increases, with the largest haloes associated with the most evolved Li-mica-bearing aplite-pegmatites. Li and Cs are enriched in metasedimentary host rocks furthest from the pegmatite dykes, followed by Rb and to a lesser extent by Sn, F, B, Be, and Tl.

6) For mineral exploration, concentrations higher than 200 ppm Li, 30 ppm Cs, 300 ppm Rb, and 15 ppm Sn in regional metasediments are indicators for proximity to an evolved aplite-pegmatite. Highly metasomatized host rocks, with maximum absolute gains of up to ~4000 ppm Li, ~1300 ppm Cs, ~1300 ppm Rb, and 170 ppm Sn could indicate the presence of multiple evolved dykes. In contrast, highly chloritized metasedimentary samples, with high CIA (>70) and LOI (>3 wt%) values, should be treated with caution. Samples with pervasive chloritization may have experienced an alteration process that postponed pegmatite-related metasomatism and caused leaching of previously enriched elements.

7) The present study suggests that the Fregeneda–Almendra Pegmatite Field is a suitable area to improve innovative less-invasive methods for critical mineral resource exploration.

Declaration of Competing Interest

The authors declare that they have no known competing financial interests or personal relationships that could have appeared to influence the work reported in this paper.

Data availability

Data will be made available on request.

Acknowledgements

Appendix A. Supplementary data

Supplementary data to this article can be found online at https://doi.org/10.1016/j.oregeorev.2022.105155.

References

Ague, J.J., 1994. Mass transfer during Barrovian metamorphism of pelites, south-central Connecticut. I: Evidence for changes in composition and volume. Am. J. Sci. 294, 989–1057. https://doi.org/10.2475/ajs.294.8.989.

Antunes, I.M.H.R., Neiva, A.M.R., Farinha Ramos, J.M., Silva, P.B., Silva, M.M.V.G., Corfu, F., 2013. Petrogenetic links between lepidolite-subtype aplite-pegmatite, aplite veins and associated granites at Segura (central Portugal). Chem. Erde Geochem. 73, 323–341. https://doi.org/10.1016/j.chemer.2012.12.003.

Audétat, A., 2019. The Metal Content of Magmatic-Hydrothermal Fluids and Its Relationship to Mineralization Potential. Econ. Geol. 114, 1033–1056. https://doi.org/10.5382/econgeo.4673.

Audétat, A., Pettke, A., Heinrich, C.A., Bodnar, R.J., 2008. The Composition of Magmatic-Hydrothermal Fluids in Barren and Mineralized Intrusions. Econ. Geol. 103, 877–908. https://doi.org/10.2113/gsecongeo.103.5.877.

Ballouard, C., Elburg, M.A., Tappe, S., Reinke, C., Ueckermann, H., Doggart, S., 2020. Magmatic-hydrothermal evolution of rare metal pegmatites from the Mesoproterozoic Orange River pegmatite belt (Namaqualand, South Africa). Ore Geol. Rev. 116, 103252 https://doi.org/10.1016/j.oregeorev.2019.103252.

Barros, R., Kaeter, D., Menuge, J.F., Škoda, R., 2020. Controls on chemical evolution and rare element enrichment in crystallising albite-spodumene pegmatite and wallrocks: Constraints from mineral chemistry. Lithos 352–353, 105289. https://doi.org/10.1016/j.lithos.2019.105289.

Bartels, A., Vetere, F., Holtz, F., Behrens, H., Linnen, R.L., 2011. Viscosity of flux-rich pegmatitic melts. Contrib. Mineral. Petrol. 162, 51–60. https://doi.org/10.1007/s00410-010-0582-3.

Bea, F., Pereira, M.D., Corretgé, L.G., Fershtater, G.B., 1994. Differentiation of strongly peraluminous, perphosphorous granites: the Pedrobernardo pluton, central Spain. Geochim. Cosmochim. Acta 58, 2609–2628. https://doi.org/10.1016/0016-7037(94)90132-5.

Bea, F., Montero, P., González-Lodeiro, F., Talavera, C., 2007. Zircon inheritance reveals exceptionally fast crustal magma generation processes in Central Iberia during the Cambro-Ordovician. J. Petrol. 48, 2327–2339. https://doi.org/10.1093/petrology/egm061.

Beinlich, A., Klemd, R., John, T., Gao, J., 2010. Trace-element mobilization during Ca-metasomatism along a major fluid conduit: Eclogitization of blueschist as a consequence of fluid–rock interaction. Geochim. Cosmochim. Acta 74, 1892–1922. https://doi.org/10.1016/j.gca.2009.12.011.

Bibienne, T., Magnan, J.-F., Rupp, A., Laroche, N., 2020. From Mine to Mind and Mobiles: Society's Increasing Dependence on Lithium. Elements 16, 265–270. https://doi.org/10.2138/gselements.16.4.265.

Binder, B., Wenzel, T., Keppler, H., 2018. The partitioning of sulfur between multicomponent aqueous fluids and felsic melts. Contrib. Mineral. Petrol. 173, 18. https://doi.org/10.1007/s00410-018-1445-6.

Blengini, G.A., Latunussa, C.E.L., Eynard, U., Torres de Matos, C., Wittmer, D., Georgitzikis, K., Pavel, C., Carrara, S., Mancini, L., Unguru, M., Blagoeva, D., Mathieux, F., Pennington, D., 2020. Study on the EU's list of Critical Raw Materials Final Report. European Commission. https://doi.org/10.2873/11619.

Cardoso-Fernandes, J., Teodoro, A.C., Lima, A., 2019. Remote sensing data in lithium (Li) exploration: A new approach for the detection of Li-bearing pegmatites. Int. J. Appl. Earth Obs. Geoinf. 76, 10–25. https://doi.org/10.1016/j.jag.2018.11.001.

Cardoso-Fernandes, J., Teodoro, A.C., Lima, A., Perrotta, M., Roda-Robles, E., 2020. Detecting Lithium (Li) Mineralizations from Space: Current Research and Future Perspectives. Appl. Sci. 10, 1785. https://doi.org/10.3390/app10051785.

Cardoso-Fernandes, J., Lima, J., Lima, A., Roda-Robles, E., Köhler, M., Schaefer, S., Barth, A., Knobloch, A., Gonçalves, M.A., Gonçalves, F., Teodoro, A.C., 2022. Stream sediment analysis for Lithium (Li) exploration in the Douro region (Portugal): A comparative study of the spatial interpolation and catchment basin approaches. J. Geochem. Explor. 236, 106978 https://doi.org/10.1016/j.gexplo.2022.106978.

Carrington da Costa, M., 1950. Notícia sobre uma carta geológica do Buçaco de Nery Delgado. Comun. Serv. Geo. Port, 1–28.

Černý, P., Ercit, T.S., 2005. The classification of granitic pegmatites revisited. Can. Mineral. 43, 2005–2026. https://doi.org/10.2113/gscanmin.43.6.2005.

Černý, P., 1989. Exploration strategy and methods for pegmatite deposits of tantalum. In: Möller, P., Černý, P., Saupé, F., eds. Lanthanides, Tantalum and Niobium. Springer-Verlag, Berlin, 274–302. 10.1007/978-3-642-87262-4.

Charoy, B., Noronha, F., Lima, A., 2001. Spodumene-petalite-eucryptite: mutual relationships and pattern of alteration in Li-rich aplite-pegmatite dykes from northern Portugal. Can. Mineral. 39, 729–746. https://doi.org/10.2113/gscanmin.39.3.729.

Debon, F., Le Fort, P., 1983. A chemical–mineralogical classification of common plutonic rocks and associations. Trans. R. Soc. Edinburgh: Earth Sci. 73, 135–149. https://doi.org/10.1017/S0263593300010117.

Dias da Silva, Í., Gómez-Barreiro, J., Martínez Catalán, J.R., Ayarza, P., Pohl, J., Martínez, E., 2017. Structural and microstructural analysis of the Retortillo Syncline (Variscan belt, Central Iberia). Implications for the Central Iberian Orocline. Tectonophysics 717, 99–115. https://doi.org/10.1016/j.tecto.2017.07.015.

Dias da Silva, Í., 2014. Geología de las Zonas Centro Ibérica y Galicia-Trás-os-Montes en la parte oriental del Complejo de Morais, Portugal/España. PhD Thesis. Salamanca, Univ. Salamanca, 424 pp.

Dias, G., Leterrier, J., Mendes, A., Simões, P.P., Bertrand, J.M., 1998. U-Pb zircon and monazite geochronology of post-collisional Hercynian granitoids from the Central Iberian Zone (Northern Portugal). Lithos 45, 349–369. https://doi.org/10.1016/S0024-4937(98)00039-5.

Díez Fernández, R., Pereira, M.F., 2016. Extensional orogenic collapse captured by strike-slip tectonics: Constraints from structural geology and U-Pb geochronology of the Pinhel shear zone (Variscan orogen, Iberian Massif). Tectonophysics 691, 290–310. https://doi.org/10.1016/j.tecto.2016.10.023.

Díez Fernández, R., Pereira, M.F., 2017. Strike-slip shear zones of the Iberian Massif: Are they coeval? Lithosphere 9, 726–744. https://doi.org/10.1130/L648.1.

Escuder Viruete, J., Arenas, R., Martínez Catalán, J.R., 1994. Tectonothermal evolution associated with Variscan crustal extension in the Tormes Gneiss Dome (NW Salamanca, Iberian Massif, Spain). Tectonophysics 238, 117–138. https://doi.org/10.1016/0040-1951(94)90052-3.

Estrade, G., Salvi, S., Béziat, D., Williams-Jones, A.E., 2015. The Origin of Skarn-Hosted Rare-Metal Mineralization in the Ambohimirahavavy Alkaline Complex. Madagascar. Econ. Geol. 110, 1485–1513. https://doi.org/10.2113/econgeo.110.6.1485.

Fabre, C., Ourti, N.E., Mercadier, J., Cardoso-Fernandes, J., Dias, F., Perrotta, M., Koerting, F., Lima, A., Kaestner, F., Koellner, N., Linnen, R., Benn, D., Martins, T., Cauzid, J., 2021. Analyses of Li-Rich Minerals Using Handheld LIBS Tool. Data 6, 68. https://doi.org/10.3390/data6060068.

Fedo, C., Nesbitt, H.W., Young, G.M., 1995. Unraveling the effects of potassium metasomatism in sedimentary rocks and paleosols, with implications for paleoweathering conditions and provenance. Geology 23, 921–924. https://doi.org/10.1130/0091-7613(1995)023<0921:UTEOPM<2.3.CO;2.

Ferreira, J.A., Bento dos Santos, T., Pereira, I., Mata, J., 2019. Tectonically assisted exhumation and cooling of Variscan granites in an anatectic complex of the Central Iberian Zone, Portugal: constraints from LA-ICP-MS zircon and apatite U-Pb ages. Int. J. Earth Sci. 108, 2153–2175. https://doi.org/10.1007/s00531-019-01755-1.

Ferreira, J.A., Mata, J., Bento dos Santos, T., Pereira, I., 2020. The role of melting on the geochemical evolution and isotopic variability of an anatectic complex in the Iberian Variscides. Lithos 378–379, 105769. https://doi.org/10.1016/j.lithos.2020.105769.

Fuchsloch, W.C., Nex, P.A.M., Kinnaird, J.A., 2019. The geochemical evolution of Nb-Ta-Sn oxides from pegmatites of the Cape Cross-Uis pegmatite belt. Namibia. Mineral. Mag. 83, 161–179. https://doi.org/10.1180/mgm.2018.151.

Fuenlabrada, J.M., Pieren, A.P., Díez Fernández, R., Sánchez Martínez, S., Arenas, R., 2016. Geochemistry of the Ediacaran-Early Cambrian transition in Central Iberia: Tectonic setting and isotopic sources. Tectonophysics 681, 15–30. https://doi.org/10.1016/j.tecto.2015.11.013.

Fuenlabrada, J.M., Arenas, R., Sánchez Martínez, S., Díez Fernández, R., Pieren, A.P., Pereira, M.F., Chichorro, M., Silva, J.B., 2020. Geochemical and isotopic (Sm–Nd) provenance of Ediacaran-Cambrian metasedimentary series from the Iberian Massif. Paleoreconstruction of the North Gondwana margin. Earth Sci. Rev. 201, 103079 https://doi.org/10.1016/j.earscirev.2019.103079.

Fuenlabrada, J.M., Arenas, R., Díez Fernández, R., González del Tánago, J., Martín-Parra, L.M., Matas, J., Rojo-Pérez, E., Sánchez Martínez, S., Andonaegui, P., Solis Alulima, B., 2021. Tectonic setting and isotopic sources (Sm–Nd) of the SW Iberian Autochthon (Variscan Orogen). J. Iber. Geol. 47, 121–150. https://doi.org/10.1007/s41513-020-00148-7.

Fuertes-Fuente, M., Martin-Izard, A., 1998. The Forcarei Sur rare-element granitic pegmatite field and associated mineralization, Galicia. Spain. Can. Mineral. 36, 303–325.

Galeschuk, C., Vanstone, P., 2007. Exploration Techniques for Rare Element Pegmatite in the Bird River Greenstone Belt, Southeastern Manitoba. In: Milkereit, B., (Ed.), Proceedings of Exploration 07: Fifth Decennial Conference on Mineral Exploration. Toronto, Canada, pp. 823–839.

Garate-Olave, I., Müller, A., Roda-Robles, E., Gil-Crespo, P.P., Pesquera, A., 2017. Extreme fractionation in a granite–pegmatite system documented by quartz chemistry: The case study of Tres Arroyos (Central Iberian Zone, Spain). Lithos 286, 162–164. https://doi.org/10.1016/j.lithos.2017.06.009.

Garate-Olave, I., Roda-Robles, E., Gil-Crespo, P.P., Pesquera, A., Errandonea-Martin, J., 2020. The Tres Arroyos Granitic Aplite-Pegmatite Field (Central Iberian Zone, Spain): Petrogenetic Constraints from Evolution of Nb-Ta-Sn Oxides. Whole-Rock Geochemistry and U-Pb Geochronology. Minerals 10, 1008. https://doi.org/10.3390/min10111008.

García-Arias, M., Díez-Montes, A., Villaseca, C., Blanco-Quintero, I.F., 2018. The Cambro-Ordovician Ollo de Sapo magmatism in the Iberian Massif and its Variscan evolution: A review. Earth Sci. Rev. 176, 345–372. https://doi.org/10.1016/j.earscirev.2017.11.004.

Gourcerol, B., Gloaguen, E., Melleton, J., Tuduri, J., Galiegue, X., 2019. Re-assessing the European lithium resource potential – A review of hard-rock resources and metallogeny. Ore Geol. Rev. 109, 494–519. https://doi.org/10.1016/j.oregeorev.2019.04.015.

Grant, J.A., 1986. The Isocon Diagram—A Simple Solution to Gresen's Equation for Metasomatic Alteration. Econ. Geol. 81, 1976–1982. https://doi.org/10.2113/gsecongeo.81.8.1976.

Grant, J.A., 2005. Isocon analysis: A brief review of the method and applications. Phys. Chem. Earth. 30, 997–1004. https://doi.org/10.1016/j.pce.2004.11.003.

Gresens, R.L., 1967. Composition–volume relationships of metasomatism. Chem. Geol. 2, 47–55. https://doi.org/10.1016/0009-2541(67)90004-6.

Gutiérrez-Alonso, G., Fernández-Suárez, J., Jeffries, T.E., Jenner, G.A., Tubrett, M.N., Cox, R., Jackson, S.E., 2003. Terrane accretion and dispersal in the northern Gondwana margin. An Early Paleozoic analogue of a long-lived active margin. Tectonophysics 365, 221–232. https://doi.org/10.1016/S0040-1951(03)00023-4.

Gutiérrez-Alonso, G., Fernández-Suárez, J., Jeffries, T.E., Johnston, S.T., Pastor-Galán, D., Murphy, J.B., Franco, M.P., Gonzalo, J.C., 2011. Diachronous post-orogenic magmatism within a developing orocline in Iberia, European Variscides. Tectonics 30, TC5008. https://doi.org/10.1029/2010TC002845.

Herron, M.M., 1988. Geochemical classification of terrigenous sands and shales from core or log data. J. Sediment. Petrol. 58, 820–829. https://doi.org/10.1306/212F8E77-2B24-11D7-8648000102C1865D.

Hulsbosch, N., Boiron, M.C., Dewaele, S., Muchez, P., 2016. Fluid fractionation of tungsten during granite–pegmatite differentiation and the metal source of peribatholitic W quartz veins: Evidence from the Karagwe-Ankole Belt (Rwanda). Geochim. Cosmochim. Acta 175, 299–318. https://doi.org/10.1016/j.gca.2015.11.020.

Hulsbosch, N., Muchez, P., 2020. Tracing fluid saturation during pegmatite differentiation by studying the fluid inclusion evolution and multiphase cassiterite mineralisation of the Gatumba pegmatite dyke system (NW Rwanda). Lithos 354–355, 105285. https://doi.org/10.1016/j.lithos.2019.105285.

Jaskula, B.W., 2017. Minerals Yearbook: Lithium. U.S. Geol, Surv.

Julivert, M., Marcos, A., Truyols, J., 1972. L'évolution paléogéographique du NW de l'Espagne pendant l'Ordovicien-Silurien. Bull. Soc. Geol. Mineral. Bretagne 4, 1–7.

Kaeter, D., Barros, R., Menuge, J.F., Chew, D.M., 2018. The magmatic hydrothermal transition in rare-element pegmatites from southeast Ireland: LA-ICP-MS chemical mapping of muscovite and columbite-tantalite. Geochim. Cosmochim. Acta 240, 96–130. https://doi.org/10.1016/j.gca.2018.08.024.

Kaeter, D., Barros, R., Menuge, J.F., 2021. Metasomatic High Field Strength Element, Tin, and Base Metal Enrichment Processes in Lithium Pegmatites from Southeast Ireland. Econ. Geol. 116, 169–198. https://doi.org/10.5382/econgeo.4784.

Kesler, S.E., Gruber, P.W., Medina, P.A., Keoleian, G.A., Everson, M.P., Wallington, T.J., 2012. Global lithium resources: Relative importance of pegmatite, brine and other deposits. Ore Geol. Rev. 48, 55–69. https://doi.org/10.1016/j.oregeorev.2012.05.006.

Kesselring, M., Wagner, F., Kirsch, M., Ajjabou, L., Gloaguen, R., 2020. Development of Sustainable Test Sites for Mineral Exploration and Knowledge Spillover for Industry. Sustainability 12, 2016. https://doi.org/10.3390/su12052016.

Kretz, R., Hartree, R., Jones, P., 1989. Metasomatic crystallization of muscovite in granite and tourmaline in schist related to pegmatite emplacement near Yellowknife. Canada. Contrib. Mineral. Petrol. 102, 191–204. https://doi.org/10.1007/BF00375340.

Lentz, D.R., Gregoire, C., 1995. Petrology and mass-balance constraints on major-, trace-, and rare-earth-element mobility in porphyry– greisen alteration associated with the epizonal True Hill granite, southwestern New Brunswick. Canada. J. Geochem. Explor. 52, 303–331. https://doi.org/10.1016/0375-6742(94)00059-K.

Linnen, R.L., Van Litchervelde, M., Černý, P., 2012. Granitic pegmatites as sources of strategic metals. Elements 8, 275–280. https://doi.org/10.2113/gselements.8.4.275.

London, D., 1986. The magmatic-hydrothermal transition in the Tanco rare-element pegmatite: evidence from fluid inclusions and phase equilibrium experiments. Am. Mineral. 71, 376–395.

London, D., 1987. Internal differentiation of rare-element pegmatites: Effects of boron, phosphorus, and fluorine. Geochim. Cosmochim. Acta 51, 403–420. https://doi.org/10.1016/0016-7037(87)90058-5.

London, D., 2018. Ore-forming processes within granitic pegmatites. Ore Geol. Rev. 101, 349–383. https://doi.org/10.1016/j.oregeorev.2018.04.020.

López-Moro, F.J., 2012. EASYGRESGRANT—A Microsoft Excel spreadsheet to quantity volume change and to perform mass-balance modeling in metasomatic systems. Comput. Geosci. 39, 191–196. https://doi.org/10.1016/j.cageo.2011.07.014.

López-Moro, F.J., López-Plaza, M., 2004. Monzonitic series from the Variscan Tormes Dome (Central Iberian Zone): petrogenetic evolution from monzogabbro to granite magmas. Lithos 72, 19–44. https://doi.org/10.1016/j.lithos.2003.08.002.

López-Moro, F.J., Romer, R.L., López-Plaza, M., Gónzalez Sánchez, M., 2017. Zircon and allanite U-Pb ID-TIMS ages of vaugnerites from the Calzadilla pluton, Salamanca (Spain): dating mantle-derived magmatism and post-magmatic subsolidus overprint. Geol. Acta 15, 395–408. https://doi.org/10.1344/GeologicaActa2017.15.4.9.

López-Moro, F.J., López-Plaza, M., Gutiérrez-Alonso, G., Fernández-Suárez, J., López-Carmona, A., Hofmann, M., Romer, R.L., 2018. Crustal melting and recycling: geochronology and sources of Variscan syn-kinematic anatectic granitoids of the Tormes Dome (Central Iberian Zone). A U-Pb LA-ICP-MS study. Int. J. Earth Sci. 107, 985–1004. https://doi.org/10.1007/s00531-017-1483-8.

López-Plaza, M., Carnicero, A., Gonzalo, J.C., 1982. Estudio geológico del campo filoniano de la Fregeneda (Salamanca). Stud. Geol. Salmanticensia 17, 89–98.

Márquez-Zavalía, M.F., Galliski, M.Á., Černý, P., Chapman, R., 2012. An assemblage of bismuth-rich, tellurium-bearing minerals in the El Quemado granitic pegmatite, Nevados de Palermo, Salta. Argentina. Can. Mineral. 50, 1489–1498. https://doi.org/10.3749/canmin.50.6.1489.

Martínez Catalán, J.R., Rubio Pascual, F.J., Díez Montes, A., Díez Fernández, R., Gómez Barreiro, J., Dias da Silva, I., González Clavijo, E., Ayarza, P., Alcock, J.E., 2014. The late Variscan HT/LP metamorphic event in NW and Central Iberia: relationships to

crustal thickening, extension, orocline development and crustal evolution. In: Schulmann, K., Martínez Catalán, J.R., Lardeaux, J.M., Janousek, V., Oggiano, G. (Eds.), the Variscan Orogeny: Extent, Timescale and the Formation of the European Crust. Geol. Soc. Spec. Publ, London, pp. 225–247. https://doi.org/10.1144/SP405.1.

Martínez Catalán, J.R., Schulmann, K., Ghienne, J.-F., 2021. The Mid-Variscan Allochthon: Keys from correlation, partial retrodeformation and plate-tectonic reconstruction to unlock the geometry of a non-cylindrical belt. Earth Sci. Rev. 220 https://doi.org/10.1016/j.earscirev.2021.103700.

Martins, T., Roda-Robles, E., Lima, A., Parseval, P., 2012. Geochemistry and evolution of micas in the Barroso-Alvão pegmatite field, northern Portugal. Can. Mineral. 50, 1117–1129. https://doi.org/10.3749/canmin.50.4.1117.

Martins, T., Linnen, R.L., Fedikow, M.A.F., Singh, J., 2017. Whole-rock and mineral geochemistry as exploration tools for rare-element pegmatite in Manitoba: examples from the Cat Lake-Winnipeg River and Wekusko Lake pegmatite fields (parts of NTS 52L6, 63J13). In: Report of Activities 2017. Manitoba Growth, Enterprise and Trade, Manitoba Geological Survey, pp. 42–51.

McDonough, W.F., Sun, S.-S., 1995. The composition of the Earth. Chem. Geol. 120, 223–253. https://doi.org/10.1016/0009-2541(94)00140-4.

McLennan, S.M., 1993. Weathering and Global Denudation. J. Geol. 101, 295–303. https://doi.org/10.1086/648222.

Migdisov, A.A., Williams-Jones, A.E., 2014. Hydrothermal transport and deposition of the rare earth elements by fluorine-bearing aqueous liquids. Miner. Deposita 49, 987–997. https://doi.org/10.1007/s00126-014-0554-z.

Morgan VI, G.B., London, D., 1987. Alteration of amphibolitic wallrocks around the Tanco rare-element pegmatite, Bernic Lake. Manitoba. Am. Mineral. 72, 1097–1121.

Müller, A., Reimer, W., Wall, F., Williamson, B., Menuge, J., Brönner, M., Haase, C., Brauch, K., Pohl, C., Lima, A., Teodoro, A., Cardoso-Fernandes, J., Roda-Robles, E., Harrop, J., Smith, K., Wanke, D., Unterweissacher, T., Hopfner, M., Schröder, M., Clifford, B., Moutela, P., Lloret, C., Ranza, L., Rausa, A., 2022. GREENPEG – exploration for pegmatite minerals to feed the energy transition: first steps towards the Green Stone Age. Geol. Soc. London Spec. Publ. 526, 27. https://doi.org/10.1144/SP526-2021-189.

Nabelek, P.I., Whittington, A.G., Sirbescu, M.-L.-C., 2010. The role of H_2O in rapid emplacement and crystallization of granite pegmatites: resolving the paradox of large crystals in highly undercooled melts. Contrib. Mineral. Petrol. 160, 313–325. https://doi.org/10.1007/s00410-009-0479-1.

Neiva, A.M.R., Ramos, J.M.F., 2010. Geochemistry of granitic aplite-pegmatite sills and petrogenetic links with granites, Guarda-Belmonte area, central Portugal. Eur. J. Mineral. 22, 837–854. https://doi.org/10.1127/0935-1221/2010/0022-2072.

Neiva, A.M.R., Silva, P.B., Ramos, J.M.F., 2012. Geochemistry of granitic aplite-pegmatite veins and sills and their minerals from the Sabugal area, central Portugal. N. Jb. Miner. Abh. 189, 49–74. https://doi.org/10.1127/0077-7757/2011/0209.

Nesbitt, H.W., Young, G.M., 1982. Early Proterozoic climates and plate motions inferred from major element chemistry of lutites. Nature 299, 715–717. https://doi.org/10.1038/299715a0.

Pell, R., Tijsseling, L., Goodenough, K., Wall, F., Dehaine, Q., Grant, A., Deak, D., Yan, X., Whattoff, P., 2021. Towards sustainable extraction of technology materials through integrated approaches. Nat. Rev. Earth Environ. 2, 665–679. https://doi.org/10.1038/s43017-021-00211-6.

Pereira, M.F., Díez Fernández, R., Gama, C., Hofmann, M., Gärtner, A., Linnemann, U., 2018. S-type granite generation and emplacement during a regional switch from extensional to contractional deformation (Central Iberian Zone, Iberian autochthonous domain, Variscan Orogeny). Int. J. Earth Sci. 107, 251–267. https://doi.org/10.1007/s00531-017-1488-3.

Pérez-Soba, C., Villaseca, C., 2019. Li-Na-metasomatism related to I-type granite magmatism: A case study of the highly fractionated La Pedriza pluton (Iberian Variscan belt). Lithos 344–345, 159–174. https://doi.org/10.1016/j.lithos.2019.06.008.

Pesquera, A., Roda-Robles, E., Gil-Crespo, P.P., Valls, D., Torres-Ruiz, J., 2020. The metasomatic enrichment of Li in psammopelitic units at San José-Valdeflórez, Central Iberian Zone, Spain: a new type of lithium deposit. Sci. Rep. 10, 10828. https://doi.org/10.1038/s41598-020-67520-6.

Pollard, P.J., Pichavant, M., Charoy, B., 1987. Contrasting evolution of fluorine- and boron-rich tin systems. Miner. Deposita 22, 315–321. https://doi.org/10.1007/BF00204525.

Potdevin, J.L., 1993. Gresens 92: a simple Macintosh program of the Gresens method. Comput. Geosci. 19, 1229–1238. https://doi.org/10.1016/0098-3004(93)90027-3.

Raith, J.G., Riemer, née Schöner, N., Meisel, T.,, 2004. Boron metasomatism and behaviour of rare earth elements during formation of tourmaline rocks in the eastern Arunta Inlier, central Australia. Contrib. Mineral. Petrol. 147, 91–109. https://doi.org/10.1007/s00410-003-0548-9.

Roda-Robles, E., Pesquera, A., Velasco, F., 1995. Micas of the muscovite-lepidolite series from the Fregeneda pegmatites (Salamanca, Spain). Mineral. Petrol. 55, 145–157.

Roda-Robles, E., Fontan, F., Pesquera, A., Velasco, F., 1996. The phosphate mineral association of the granitic pegmatites of the Fregeneda area (Salamanca, Spain). Mineral. Mag. 60, 767–778. https://doi.org/10.1180/minmag.1996.060.402.06.

Roda-Robles, E., Pesquera Pérez, A., Velasco Roldán, F., Fontan, F., 1999. The granitic pegmatites of the Fregeneda area (Salamanca, Spain): characteristics and petrogenesis. Mineral. Mag. 63, 535–558. https://doi.org/10.1180/002646199548709.

Roda-Robles, E., Vieira, R., Pesquera, A., Lima, A., 2010. Chemical variations and significance of phosphates from the Fregeneda-Almendra pegmatite field, Central Iberian Zone (Spain and Portugal). Mineral. Petrol. 100, 23–34. https://doi.org/10.1007/s00710-010-0117-7.

Roda-Robles, E., Pesquera, A., Gil-Crespo, P.P., Vieira, R., Lima, A., Garate-Olave, I., Martins, T., Torres-Ruiz, J., 2016. Geology and mineralogy of Li mineralization in the Central Iberian Zone (Spain and Portugal). Mineral. Mag. 80, 103–126. https://doi.org/10.1180/minmag.2016.080.049.

Roda-Robles, E., Villaseca, C., Pesquera, A., Gil-Crespo, P.P., Vieira, R., Lima, A., Garate-Olave, I., 2018. Petrogenetic relationships between variscan granitoids and Li–(F–P)-rich aplite-pegmatites in the Central Iberian Zone: geological and geochemical constraints and implications for other regions from the European variscides. Ore Geol. Rev. 95, 408–430. https://doi.org/10.1016/j.oregeorev.2018.02.027.

Rodríguez Fernández, L.R., Díez Montes, A., Escuder, J., Carrasco, A., 2000. Hoja geológica número 448 (Vilvestre). Mapa Geológico de España a Escala 1:50.000 (2ª serie). Madrid: Inst. Geol. Miner. Es. Retrieved from http://info.igme.es/cartografiadigital/geologica/Magna50Hoja.aspx?intranet=false&id=448B.

Rodríguez Fernández, L.R., Oliveira, J.T., 2015. Mapa geológico de España y Portugal a escala 1: 1.000.000. Inst. Geol. Miner. Es. Laboratório Nacional de Energia e Geologia de Portugal. http://info.igme.es/cartografiadigital/geologica/Geologicos1MMapa.aspx?Id=Geologico1000_(2015.

Rodríguez-Alonso, M.D., Peinado, M., López-Plaza, M., Franco, P., Carnicero, A., Gonzalo, J.C., 2004. Neoproterozoic-Cambrian synsedimentary magmatism in the Central Iberian Zone (Spain): geology, petrology and geodynamic significance. Int. J. Earth Sci. 93, 897–920. https://doi.org/10.1007/s00531-004-0425-4.

Rojo-Pérez, E., Fuenlabrada, J.M., Linnemann, U., Arenas, R., Sánchez Martínez, S., Díez Fernández, R., Martín Parra, L.M., Matas, J., Andonaegui, P., Fernández-Suárez, J., 2021. Geochemistry and Sm–Nd isotopic sources of Late Ediacaran siliciclastic series in the Ossa-Morena Complex: Iberian-Bohemian correlations. Int. J. Earth Sci. 110, 467–485. https://doi.org/10.1007/s00531-020-01963-0.

Roza-Llera, A., Fuertes-Fuente, M., Cepedal, A., Martin-Izard, A., 2019. Barren and Li–Sn–Ta Mineralized Pegmatites from NW Spain (Central Galicia): A Comparative Study of Their Mineralogy, Geochemistry, and Wallrock Metasomatism. Minerals 9, 739. https://doi.org/10.3390/min9120739.

Rudnick, R.L., Gao, S., 2014. Composition of the continental crust. In: Holland, H.D., Turekian, K.K. (Eds.), Treatise on Geochemistry, 2nd edition Volume 4: The Crust. Elsevier Science, Oxford, pp. 1–51. https://doi.org/10.1016/B978-0-08-095975-7.00301-6.

Ruiz-Coupeau, S., Jürgens, B., Keßelring, M., Herrero-Solana, V., 2020. Sustainability in Mineral Exploration—Exploring Less Invasive Technologies via Patent Analysis. Sustainability 12, 9761. https://doi.org/10.3390/su12229761.

Selway, J.B., Breaks, F.W., Tindle, A.G., 2005. A Review of Rare-Element (Li-Cs-Ta) Pegmatite Exploration Techniques for the Superior Province, Canada, and Large Worldwide Tantalum Deposits. Explor. Min. Geol. 14, 1–4. https://doi.org/10.2113/gsemg.14.1-4.1.

Shand, S.J., 1943. Eruptive Rocks. Their Genesis, Composition, Classification, and Their Relation to Ore-Deposits with a Chapter on Meteorite. John Wiley and Sons, New York.

Shaw., R.A., Goodenough, K.M., Deady, E., Nex, P., Ruzvidzo, B., Rushton, J.C., Mounteney, I.,, 2022. The Magmatic-Hydrothermal Transition in Lithium Pegmatites: Petrographic and Geochemical Characteristics of Pegmatites from the Kamativi Area. Zimbabwe. Can. Mineral. 60, 1–31. https://doi.org/10.3749/canmin.2100032.

Shearer, C.K., Papike, J.J., Simon, S.B., Laul, J.C., Christian, R.P., 1984. Pegmatite/wallrock interactions, Black Hills, South Dakota: Progressive boron metasomatism adjacent to the Tip Top pegmatite. Geochim. Cosmochim. Acta 48, 2563–2579. https://doi.org/10.1016/0016-7037(84)90306-5.

Shearer, C.K., Papike, J.J., Simon, S.B., Laul, J.C., 1986. Pegmatite-wallrock interactions, Black Hills, South Dakota: interaction between pegmatite-derived fluids and quartz-mica schist wallrock. Am. Mineral. 71, 518–539.

Silva, A.F., Ribeiro, M.L., 1994. Notícia explicativa da folha 15-B (Freixo de Espada à Cinta) da Carta Geológica de Portugal à Escala 1:50.000. Inst. Geol. Miner Pt.

Simmons, W.B., Webber, K.L., 2008. Pegmatite genesis: state of the art. Eur. J. Mineral. 20, 421–438. https://doi.org/10.1127/0935-1221/2008/0020-1833.

Simon, A.C., Pettke, T., Candela, P.A., Piccoli, P.M., Heinrich, C.A., 2007. The partitioning behavior of As and Au in S-free and S-bearing magmatic assemblages. Geochim. Cosmochim. Acta 71, 1764–1782. https://doi.org/10.1016/j.gca.2007.01.005.

Sirbescu, M.-L.-C., Hartwick, E.E., Student, J.J., 2008. Rapid crystallization of the Animikie Red Ace Pegmatite, Florence county, northeastern Wisconsin: inclusion microthermometry and conductive-cooling modeling. Contrib. Mineral. Petrol. 156, 289–305. https://doi.org/10.1007/s00410-008-0286-0.

Sousa, M.B., 1982. Litoestratigrafia e estrutura do Complexo Xisto-Grauváquico – Grupo do Douro (NE de Portugal). PhD Thesis. Coimbra, Univ. Coimbra, unpublished, 222 pp.

Talavera, C., Montero, P., Martínez Poyatos, D., Williams, I.S., 2012. Ediacaran to Lower Ordovician age for rocks ascribed to the Schist-Graywacke Complex (Iberian Massif, Spain): Evidence from detrital zircon SHRIMP U-Pb geochronology. Gondwana Res. 22, 928–942. https://doi.org/10.1016/j.gr.2012.03.008.

Taylor, S.R., McLennan, S.M., 1985. The Continental Crust: Its Composition and Evolution. Blackwell Scientific Publications, Oxford.

Teixeira, R.J.S., Neiva, A.M.R., Silva, P.B., Gomes, M.E.P., Andersen, T., Ramos, J.M., 2011. Combined U-Pb geochronology and Lu–Hf isotope systematics by LAM–ICPMS of zircons from granites and metasedimentary rocks of Carrazeda de Ansiães and Sabugal areas, Portugal, to constrain granite sources. Lithos 125, 321–334. https://doi.org/10.1016/j.lithos.2011.02.015.

Teixeira, R.J.S., Neiva, A.M.R., Gomes, M.E.P., Corfu, F., Cuesta, A., Croudace, I.W., 2012. The role of fractional crystallization in the genesis of early syn-D_3, tin-mineralized Variscan two-mica granites from the Carrazeda de Ansiães area,

northern Portugal. Lithos 153, 177–191. https://doi.org/10.1016/j.lithos.2012.04.024.

Teng, F.Z., McDonough, W.F., Rudnick, R.L., Walker, R.J., 2006. Diffusion-driven extreme lithium isotopic fractionation in country rocks of the Tin Mountain pegmatite. Earth Planet. Sci. Lett. 243, 701–710. https://doi.org/10.1016/j.epsl.2006.01.036.

Thomas, R., Davidson, P., 2012. Water in granite and pegmatite-forming melts. Ore Geol. Rev. 46, 32–46. https://doi.org/10.1016/j.oregeorev.2012.02.006.

Thomas, R., Davidson, P., 2016. Revisiting complete miscibility between silicate melts and hydrous fluids, and the extreme enrichment of some elements in the supercritical state — Consequences for the formation of pegmatites and ore deposits. Ore Geol. Rev. 72, 1088–1101. https://doi.org/10.1016/j.oregeorev.2015.10.004.

Thomas, R., Webster, J.D., Heinrich, W., 2000. Melt inclusions in pegmatite quartz: complete miscibility between silicate melts and hydrous fluids at low pressure. Contrib. Mineral. Petrol. 139, 394–401. https://doi.org/10.1007/s004100000120.

Thomas, R., Förster, H.-J., Heinrich, W., 2003. The behaviour of boron in a peraluminous granite–pegmatite system and associated hydrothermal solutions: a melt and fluid inclusion study. Contrib. Mineral. Petrol. 144, 457–472. https://doi.org/10.1007/s00410-002-0410-5.

Thomas, R., Davidson, P., Beurlen, H., 2012. The competing models for the origin and internal evolution of granitic pegmatites in the light of melt and fluid inclusion research. Mineral. Petrol. 106, 55–73. https://doi.org/10.1007/s00710-012-0212-z.

Tingle, T., Fenn, P.M., 1984. Transport and concentration of molybdenum in granite molybdenite systems: Effects of fluorine and sulphur. Geology 12, 156–158. https://doi.org/10.1130/0091-7613(1984)12<156:TACOMI>2.0.CO;2.

Trueman, D.L., 1978. Exploration methods in the Tanco mine area of southeastern Manitoba, Canada. Energy 3, 293–297. https://doi.org/10.1016/0360-5442(78)90025-7.

Ugidos, J.M., Valladares, M.I., Recio, C., Rogers, G., Fallick, A.E., Stephens, A.E., 1997. Provenance of Upper Precambrian-Lower Cambrian shales in the Central Iberian Zone, Spain: evidence from a chemical and isotopic study. Chem. Geol. 136, 55–70. https://doi.org/10.1016/S0009-2541(96)00138-6.

Ugidos, J.M., Valladares, M.I., Barba, P., Ellam, R.M., 2003. The Upper Neoproterozoic-Lower Cambrian of the Central Iberian Zone, Spain: chemical and isotopic (Sm–Nd) evidence that the sedimentary succession records an inverted stratigraphy of its source. Geochim. Cosmochim. Acta 67, 2615–2629. https://doi.org/10.1016/S0016-7037(03)00027-9.

Ugidos, J.M., Sánchez-Santos, J.M., Barba, P., Valladares, M.I., 2010. Upper Neoproterozoic series in the Central Iberian, Cantabrian and West Asturian Leonese Zones (Spain): geochemical data and statistical results as evidence for a shared homogenised source area. Precambrian Res. 178, 51–58. https://doi.org/10.1016/j.precamres.2010.01.009.

Valladares, M.I., Ugidos, J.M., Barba, P., Colmenero, J.R., 2002. Contrasting geochemical features of the Central Iberian Zone shales (Iberian Massif, Spain): implications for the evolution of Neoproterozoic-Lower Cambrian sediments and their sources in other peri-Gondwanan areas. Tectonophysics 352, 121–132. https://doi.org/10.1016/S0040-1951(02)00192-0.

Valle-Aguado, B., Azevedo, M.R., Schaltegger, U., Martínez Catalán, J.R., Nolan, J., 2005. U-Pb zircon and monazite geochronology of Variscan magmatism related to syn-convergence extension in Central Northern Portugal. Lithos 82, 169–184. https://doi.org/10.1016/j.lithos.2004.12.012.

Veksler, I.V., 2004. Liquid immiscibility and its role at the magmatic-hydrothermal transition: A summary of experimental studies. Chem. Geol. 210, 7–31. https://doi.org/10.1016/j.chemgeo.2004.06.002.

Vieira, R., Roda-Robles, E., Pesquera, A., Lima, A., 2011. Chemical variation and significance of micas from the Fregeneda-Almendra pegmatitic field (Central-Iberian Zone, Spain and Portugal). Am. Mineral. 96, 637–645. https://doi.org/10.2138/am.2011.3584.

Villaseca, C., Barbero, L., Herreros, V., 1998. A re-examination of the typology of peraluminous granite types in intracontinental orogenic belts. Trans. R. Soc. Edinburgh: Earth Sci. 89, 113–119. https://doi.org/10.1017/S0263593300007045.

Villaseca, C., Merino, E., Oyarzun, R., Orejana, D., Pérez-Soba, C., Chicharro, E., 2014. Contrasting chemical and isotopic signatures from Neoproterozoic metasedimentary rocks in the Central Iberian Zone (Spain) of pre-Variscan Europe: Implications for terrane analysis and early Ordovician magmatic belts. Precambrian Res. 245, 131–145. https://doi.org/10.1016/j.precamres.2014.02.006.

Villaseca, C., Merino Martínez, E., Orejana, D., Andersen, T., Belousova, E., 2016. Zircon Hf signatures from granitic orthogneisses of the Spanish Central System: Significance and sources of the Cambro-Ordovician magmatism in the Iberian Variscan Belt. Gondwana Res. 34, 60–83. https://doi.org/10.1016/j.gr.2016.03.004.

Webber, K.L., Falster, A.U., Simmons, W.B., Foord, E.E., 1997. The role of diffusion-controlled oscillatory nucleation in the formation of line rock in pegmatite-aplite dikes. J. Petrol. 38, 1777–1791. https://doi.org/10.1093/petroj/38.12.1777.

Webber, K.L., Simmons, W.B., Falster, A.U., Foord, E.E., 1999. Cooling rates and crystallization dynamics of shallow level pegmatite-aplite dikes, San Diego County. California. Am. Mineral. 84, 708–717. https://doi.org/10.2138/am-1999-5-603.

Whitney, D.L., Evans, B.W., 2010. Abbreviations for names of rock-forming minerals. American Mineralogist 95 (1), 185–187. https://doi.org/10.2138/am.2010.3371.

Xing, P., Dong, J., Yu, P., Zheng, H., Liu, X., Hu, S., Zhu, Z., 2021. Quantitative analysis of lithium in brine by laser-induced breakdown spectroscopy based on convolutional neural network. Anal. Chim. Acta 1178, 338799. https://doi.org/10.1016/j.aca.2021.338799.

Zhang, H., Tian, S., Wang, D., Li, X., Liu, T., Zhang, Y., Fu, X., Hao, X., Hou, K., Zhao, Y., Qin, Y., 2021. Lithium isotope behavior during magmatic differentiation and fluid exsolution in the Jiajika granite–pegmatite deposit, Sichuan. China. Ore Geol. Rev. 134, 104139 https://doi.org/10.1016/j.oregeorev.2021.104139.